





Hochschule Karlsruhe – Technik und Wirtschaft
Fakultät für Elektro- und Informationstechnik
Studiengang Elektrotechnik – Sensorik

BACHELORTHESIS

von

Michael Holz

Experimental Investigation of Multipacting Suppression by amorphous Carbon Coatings

Arbeitsplatz: CERN, 1211 Genf 23, Schweiz

Betreuer am Arbeitsplatz: Dr.-Ing. Friedhelm Caspers

Referent: Prof. Dr. Ulrich Grünhaupt

Korreferent: Prof. Dr. Hubert Schwab

Abgabetermin: 20.9.2012

Bachelorthesis Nr.: 113 des Studienganges Sensorik

Bearbeitet in der Zeit vom 20.06.2012 bis 20.09.2012

Abstract

The presence of electron cloud is considered as the most important limitation concerning the quality of the particle beam in the accelerators, especially with respect to the forthcoming LHC luminosity upgrade. The electron cloud can be mitigated by coating the vacuum beam chambers with thin films of low secondary electron yield (SEY). This technique is applied to two stand-alone main bending dipoles of the SPS, where the RF power is fed through a tungsten wire, stretched inside the vacuum chamber. A dipole with a bare stainless steel chamber shows a clear power threshold initiating an abrupt rise in reflected power and pressure. The effect is enhanced at RF frequencies corresponding to electron cyclotron resonances for given magnetic fields. The first results of a fully coated beam chamber do not exhibit any pressure rise or reflected RF power up to the maximum available input power. Here, reflected power has been observed only once and could not be reproduced. The results of a partially coated beam chamber show a strong reduction of multipacting. The remaining multipacting is suspected to take place outside the dipole. Several proposals for optimization of the test stand have been made.

In parallel, electron cloud measurements via the microwave transmission method have been performed during the annual scrubbing run in the SPS. These technique was successfully applied to two consecutive uncoated dipoles. Clear electron cloud signals have been observed while operating with high intensity beams and a 25 ns bunch spacing. For low intensity beams, no electron cloud could be observed. This method has proven to be very useful and the potential of a future implementation for permanent diagnostic purposes has been outlined.

Ich erkläre hiermit, dass ich die vorliegende Arbeit selbständig verfasst und keine anderen als die angegebenen Quellen und Hilfsmittel verwendet habe.

Schramberg, den 18. September 2012

Acknowledgments

I would like to thank Dr. Fritz Caspers for his excellent and very helpful supervision and for being an infinite source of ideas and wisdom in both, professional and private concerns. For encouraging me to think out of the box and for strengthening my interest in electrical engineering, especially high frequency techniques. Also many thanks for providing and organizing all the RF-related theoretical background and the equipment I needed to succeed in this project.

Many thanks to Prof. Dr. Ulrich Grünhaupt for supervising this thesis from the academical side.

Special thanks to Pedro Costa Pinto for accompanying me in „the Zone“, for many useful ideas concerning test runs, the very fruitful discussions about carbon coatings and mysterious measurement results and the discussions about what really matters in life.

Further, I would like to thank the members of our section, namely Thomas Bohl, Steven Hancock, Joachim Tueckmantel, Silke Federmann, Theodoros Argyropoulos, Juan Esteban Mueller, Luca Ficcadenti, Rama Calaga, and our section leader Elena Chapochnikova for the opportunity to present my progress at the section meetings, for a very good and constructive criticism of my work and for the overall support.

Many thanks to Mauro Taborelli for providing and sharing useful and important knowledge concerning vacuum technology and surface coatings, and for supporting me from the very beginning of my stay. Also many thanks to all remaining members of the SEY-Meetings, namely Sergio Calatroni, Paul Edwards, Holger Neupert, Wilhelmus Vollenberg, Mounir Mensi and Delphine Letant-Delrieux for the great discussions and the opportunity to learn a lot about vacuum and surface coatings.

A lot of thanks towards my friends Michael Betz, Tom Levens, Petri Leinonen, Iikka Matasaho, Janne Holma, and Krishna Bhattacharyya for awesome movie nights, BBQ parties and nice, entertaining lunch breaks.

Vielen lieben Dank an meine Eltern, die mich während meiner Arbeit, meines Studiums und meines gesamten Lebens immer für mich da waren und mich in jeder Hinsicht unterstützt haben.

If we long for our planet to be important, there is something we can do about it. We make our world significant by the courage of our questions and by the depth of our answers.

Carl Sagan, -COSMOS-

Contents

1	Introduction	1
1.1	A brief Introduction into CERN	1
1.2	The Super Proton Synchrotron	2
1.3	Motivation of this work	3
2	Basics	5
2.1	Introduction into Particle Accelerators	5
2.1.1	Electromagnetic Influence on charged Particles	5
2.1.2	Cyclotron Resonance	6
2.2	Material Science Aspects	7
2.2.1	Secondary Electron Emission	7
2.2.2	Secondary Electron Yield	8
2.2.3	Amorphous Carbon Coatings	8
2.3	The Multipacting Effect	9
2.4	Other E-Cloud Mitigation Techniques	10
2.4.1	Clearing Electrodes	10
2.4.2	Solenoids	11
2.4.3	Surface Grooves	11
2.4.4	Advantages of the Carbon Coatings	12
2.5	Electromagnetic Fields & Relativity	12
2.6	Modulation Theory	13
2.6.1	The Carrier Wave	14
2.6.2	Amplitude Modulation	14
2.6.3	Phase Modulation	16
2.6.4	Combined Modulation	17
3	The Multipacting Test Stand	19
3.1	Goal of the Experiment	19
3.2	The experimental Set-Up	19
3.3	Diagnostic Methods	21
3.4	Analysis of the electrical Circuit	22
3.5	Commissioning of the Set-up	25
3.5.1	Pump down and Leak Detection	25
3.5.2	Wire Fault Detection via Time Domain Reflectometry	25
3.5.3	Resonant Frequency Identification	27
3.5.4	Dipole Transfer Function	28
3.5.5	DC Current Heating	29
3.6	Simulations	29
3.6.1	ESA-ESTEC Multipactor Calculator	29

3.6.2	CST Microwave/Particle Studio	31
3.7	Results of the DC cylindrical Magnetron sputtered Coating	33
3.7.1	Characterization of the Stainless Steel Chamber	33
3.7.2	Coated Chamber	36
3.8	Results of the DC Hollow Cathode sputtered Coating	38
3.8.1	Characterization of the Stainless Steel Chamber	38
3.8.2	Coated Chamber	41
3.9	Spin-off Applications of the Test Stand	44
4	E-Cloud Diagnostics by Means of Microwave Transmission	47
4.1	Goal of the diagnostic Method	47
4.2	Principle	47
4.3	Set-Up 2011	49
4.4	Set-Up 2012	49
4.4.1	Results	50
5	Conclusions and Outlook	55
5.1	Multipacting Test Stand	55
5.2	Microwave Transmission Measurements	56
A	Appendix	57
	Bibliography	63

List of Figures

1.1	CERN accelerator chain	2
2.1	Architecture examples of a traveling and standing wave cavity	6
2.2	Energy distribution of electrons emitted by silver upon bombardment with 155 eV primary electrons	7
2.3	Overview of the SEY of a-C coatings and stainless steel reference sample	9
2.4	Schematic of electron cloud build up in an LHC arc beam pipe, due to photoemission and secondary emission (F. Ruggiero)	10
2.5	Electrostatic simulations of clearing electrodes	11
2.6	Electrostatic simulations of clearing electrodes	11
2.7	Principle of surface grooves and exemplary trajectories of electrons .	12
2.8	E-Field of a static point charge, a slowly moving point charge and a relativistic point charge	13
2.9	Amplitude-modulated signal in the time domain	15
2.10	Amplitude-modulated signal in the frequency domain	15
2.11	Phase-modulated signal in the time domain	17
2.12	Phase-modulated signal in the frequency domain	18
2.13	AM to PM Conversion	18
3.1	Cross section of a MBB-type chamber for SPS bending magnets . . .	20
3.2	Experimental multipacting test stand	21
3.3	Block diagram of the experimental set-up	22
3.4	Resonances of the matched resonator	23
3.5	Dual Directional Coupler	24
3.6	Transmission measurement for the backward coupling port	24
3.7	Transmission properties of the diplexer	25
3.8	Time domain reflectometry of the resonator	26

3.9	Long term evolution of the reflection coefficient	27
3.10	VNA in conventional use and with an intercalated amplifier	28
3.11	Transfer function of a reference dipole	28
3.12	Thermal outgassing	29
3.13	ESA Simulations for 130 MHz	30
3.14	ESA Simulations for 68 MHz	31
3.15	Particle tracking in the SPS camber	31
3.16	Secondary Electron Emission in particle tracking	32
3.17	Simulated particle growth rate	33
3.18	DCCMS characterization: Reflected power	34
3.19	Glow discharge and plasma formation	35
3.20	DCCMS characterization: Residual gas analysis	35
3.21	DCCMS reflected power at high external magn. fields	36
3.22	Reflected power for low and high magnetic fields on the DCCMS coated chamber	37
3.23	Pressure data of the magnetron sputtered coating	37
3.24	DCHCS characterization: Reflected power	38
3.25	Surface Conditioning	39
3.26	Pressure data during surface conditioning	39
3.27	DCHCS characterization: Reflected power with inverted magnetic fields	40
3.28	Remanent magnetic field of the chamber	40
3.29	Magnetic field with a 11 A current	41
3.30	Reflected power of the DCHCS coated chamber in the low magnetic field range	42
3.31	Pressure comparison of the uncoated and DCHCS coated chamber . .	42
3.32	Reflected power of the coated chamber at 83.86 MHz	43
3.33	Resonances used at the DCHCS coating examination	44
4.1	Vector Spectrum Analyzer Screen	48
4.2	Schematic Set-up 2011	49
4.3	Spectrogram mode of PM modulation	50
4.4	Schematic Set-up 2012	50
4.5	Phase modulated part of the spectrum for the empty machine	51

4.6	Time trace of an increased electron cloud induced signal compared to base level around -67 dB . 4 batches, 25 ns spacing and a maximum total intensity of $3455 \cdot 10^{10}$ protons.	51
4.7	Phase modulation for one batch, 25 ns spacing and a maximum total intensity of $1274 \cdot 10^{10}$ protons	52
4.8	Phase modulation for two batches, 25 ns spacing and a maximum total intensity of $2530 \cdot 10^{10}$ protons	53
4.9	Phase modulation for 3 batches, 25 ns spacing and a maximum total intensity of $3639 \cdot 10^{10}$ protons	53
A.1	Grade of the surface roughness of aluminum versus etching time . . .	57
A.2	Thermal resonance drift	58
A.3	Opened front aperture of the pre-chamber	58
A.4	Opened back aperture of the pre-chamber	59
A.5	DCCMS coating process	59
A.6	DCCMS scheme and plasma formation	60
A.7	DCHCS graphite target	60
A.8	DCHCS graphite target (inserted) and plasma formation	60
A.9	DCCMS and DCHCS morphology	61

1. Introduction

1.1 A brief Introduction into CERN

CERN is the world's largest laboratory in particle- & high-energy physics. It was founded in 1954 by famous scientists - amongst them Niels Bohr and Werner Heisenberg - and supported by eleven European governments. The idea of CERN was to bring the European nations together that have been in war over centuries, as well as to counter the emigration of scientists to other continents. Situated on the Swiss-French border, CERN today has twenty member states and a yearly budget of around 850.000.000 €. It also collaborates with non-member states. Currently, around 3000 people are employed by CERN. Additionally, over 8000 users and visiting scientists from 85 different nations work and participate in experiments and projects hosted by CERN.

CERN houses various particle accelerators from linear accelerators (e.g. LINAC2) to synchrotrons like the proton synchrotron (PS), the super proton synchrotron (SPS) and the large hadron collider (LHC). The LHC is currently the most powerful particle accelerator which collides protons and lead ions at an energy of 7 TeV and 2.76 TeV per nucleon, respectively. The enormous temperatures - namely a billion times the temperature in the center of the sun - that occur during the particle collisions, allows to reconstruct the conditions of the universe when the visible universe was not bigger than a few centimeters. The goal of the four big experiments at the LHC collision points is to investigate dark matter and to find new particles that existed before the kind of matter all things are made of now. This includes also the Higgs-Boson whose field is responsible for the inertial mass of all other particles¹ in a kind of a friction. The Higgs-Boson is the last missing particle of the standard model. The recent announcement of a newly discovered particle, which could be the Higgs-Boson, is another big step towards the verification of this model.

For realizing such huge projects, CERN always puts a lot of its effort in developing cutting-edge technology which in often leads to technology derivations shared with

¹Photons do not interact with the Higgs-field and thus are able to reach the speed of light. The reason for this is still unknown.

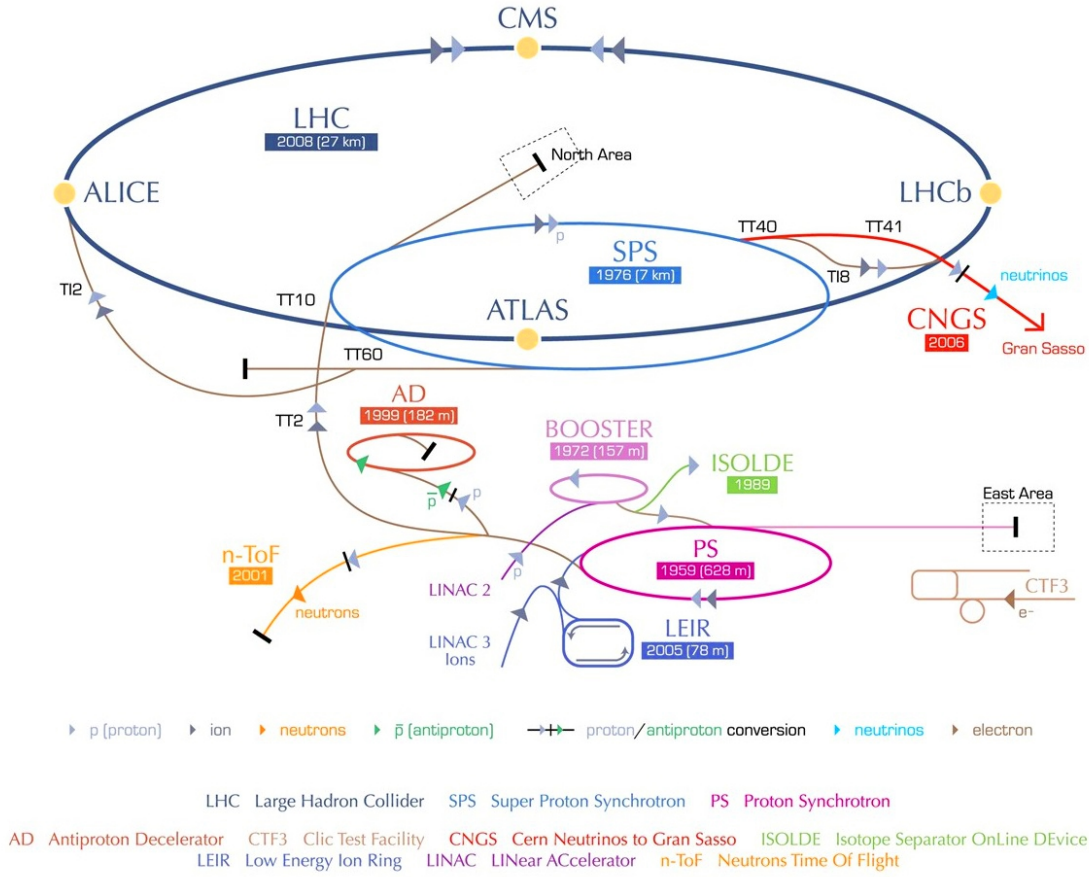


Figure 1.1: The CERN accelerator chain including the four big LHC experiments, the antiproton decelerator and smaller experiments. ©CERN 2008

the industry and consequently to humanity's benefit as a whole. Some examples are the World Wide Web (WWW), invented by Tim Berners-Lee in 1991 which was originally designed to serve as a network dedicated to particle physics. Also, the technology of particle accelerators can nowadays be found in security devices at airports and in the medical field, for example the positron-emission-tomography (PET). Considering this, it becomes clear that the whole accelerator complex is not only dedicated to physics experiments but it is also its own prototype, pushing forward practical inventions and technology.

1.2 The Super Proton Synchrotron

The SPS was commissioned in 1976 and was the largest particle accelerator at that time. It has a circumference of 6.9 km and can accelerate particle beams to a maximum energy of 400 GeV. Shortly after its commissioning, it already delivered protons to fixed-target experiments and thus provided secondary beams for additional experiments on, for example, neutrino experiments. Subsequently, the SPS was used as a proton-antiproton collider which provided first collisions in 1981. With its help, the Z and W bosons, which are the carrier particles of the weak interactions, could be discovered two years later. Also, it later provided electrons and positrons for the Large Electron Positron Collider (LEP). Today the SPS still supplies multiple experiments with different kinds of particle beams, for example the CERN Neutrino

to Gran Sasso experiment (CNGS). It is also part of the injection chain to the LHC. As particle physics pushes for more collisions in order to prove the validity of its models, a technical upgrade of the LHC and, subsequently, of the greater part of the precedent injector chain including the SPS, is necessary.

1.3 Motivation of this work

In the frame of the LHC luminosity upgrade to finally establish the high-luminosity LHC (HL-LHC) and, subsequently, provide more particle collisions, the SPS - as the last pre-accelerator before the LHC - has to face beam intensities that are way beyond the nominal intensities it was originally designed for. This upgrade involves technical problems in unprecedented extent, like the build-up of a cloud consisting of free electrons in the beam chambers. This so called electron cloud is caused by the higher beam potential and is considered as major limitation to the imminent luminosity upgrade. The presence of electron cloud causes multiple beam disturbances:

1. transverse emittance blow-up: the average spatial spread of the particles in the beam increases. This results in a reduction of luminosity. However, high luminosity is necessary to increase particle interaction when colliding two beams and is the intention of the upgrade.
2. pressure rise: since the ultra-high vacuum is not perfect, there will always be some residual gas molecules that stick to the beam pipe's surface. These gas molecules will be released due to electron-stimulated desorption, which results in a significant pressure rise in the vacuum system. The mean free path of the accelerated particles reduces, leading to beam losses. Additionally, if the pressure rises occur close to the particle detectors it will increase the noise.
3. heat load: in the cryogenic environment of the LHC, the electrons cause heat load to the beam pipe and affects the cryogenic cooling locally.

Amongst several techniques on electron cloud mitigation, that have been developed and are still in development, amorphous carbon coatings (aC-Coatings) appear to be the most promising solution. That is why this work focuses on the electron cloud mitigation by aC-Coatings and presents the development of methods to check the coatings' efficiency before the insertion in the machine and/or in the event of a large scale production.

2. Basics

2.1 Introduction into Particle Accelerators

2.1.1 Electromagnetic Influence on charged Particles

Electromagnetic fields influence charged particles like protons, ions and electrons. The Lorentz equation describes the force, which is experienced by these particles:

$$\vec{F} = q(\vec{E} + \vec{v} \times \vec{B}) \quad (2.1)$$

where \vec{F} is the experienced force, q the particle's charge, \vec{E} the electric field strength, \vec{v} the particle's velocity and \vec{B} the magnetic flux density.

Charged particles get accelerated by electric fields into or against field direction, depending on the particle's charge. The easiest way to accelerate them is to apply a DC electric field between two oppositely charged plates. This acceleration principle can be found in cathode ray tubes (CRT) and forms the basis of every old television or computer monitor. However, increasing the particle's energy continuously just by multiplying this principle is not possible, since the particles would decelerate after the second plate, facing an electric field in the wrong direction. Thus, particle accelerators operate with electric fields, alternating at radio frequencies (RF). Switching the polarity of the fields in the right moment, a quasi continuous acceleration for a bunch of particles is possible. Alternating electric fields are usually provided by cavities, powered with RF. These cavities can be implemented as traveling or standing wave structures (see figure 2.1).

Magnetic fields alone do not accelerate charged particles but bend the trajectory of already moving particles according to the Lorentz force. In circular accelerators the magnetic field is perpendicular with respect to the particle's direction of motion and thus providing a circular orbit in the accelerator. With increasing energy and velocity of the particles the magnetic field strength has to be adjusted in order to maintain the orbit. In modern, high-energy particle accelerators the maximum magnetic field strength in bending magnets can be several teslas.

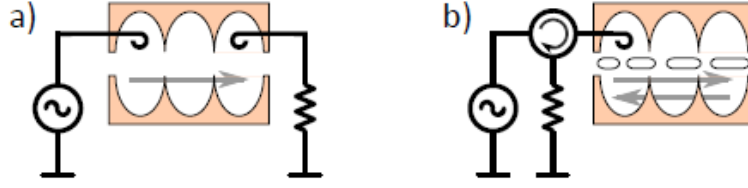


Figure 2.1: Architecture examples of a traveling (a) and standing wave (b) cavity [1].

2.1.2 Cyclotron Resonance

Cyclotron resonance is the resonant interaction between electromagnetic waves and charged particles when exposed to a DC magnetic field. In common applications like cyclotrons and circular accelerators, this field is perpendicular to the velocity vector of the particles. These particles are deflected into a circular trajectory by the Lorentz force and gain energy - proper phasing provided - when being accelerated with an alternating electric field of a certain frequency, which corresponds to the applied magnetic field. This frequency is called cyclotron frequency and can be deduced, using the equations 2.2 - 2.5:

Assuming a circular trajectory, the particles can maintain their orbit by the centripetal force which in this case is the Lorentz force. Thus, for the perpendicular case, these forces can be equated to

$$\frac{m \cdot v^2}{r} = q \cdot v \cdot B \quad (2.2)$$

where m is the particle's mass, v its tangential velocity, q its charge, B the magnetic flux density and r the radius of the circular trajectory. The tangential velocity is given by the trajectory's circumference divided by the time of revolution

$$v = \frac{2\pi r}{T} = \omega r \quad (2.3)$$

with $\omega = \frac{2\pi}{T}$, where T is the time of revolution and ω the angular velocity. Substituting this in eq. 2.2 and solving for ω , it yields

$$\omega = \frac{q \cdot B}{m} \quad (2.4)$$

or

$$f_c = \frac{q \cdot B}{2\pi \cdot m} \quad (2.5)$$

where f_c is the cyclotron frequency. A key value for cyclotron resonance with electrons as interacting particles is 28 GHz/Tesla.

2.2 Material Science Aspects

2.2.1 Secondary Electron Emission

When free, electrically charged particles, for example electrons, hit a solid surface they can liberate additional electrons from this surface, given a sufficient amount of kinetic energy. These additional electrons in the following are referred to secondary electrons, whereas the original electrons are referred to primary electrons. Figure 2.2 shows a typical energy distribution of secondary electrons which got emitted from metal surfaces (e.g. silver).

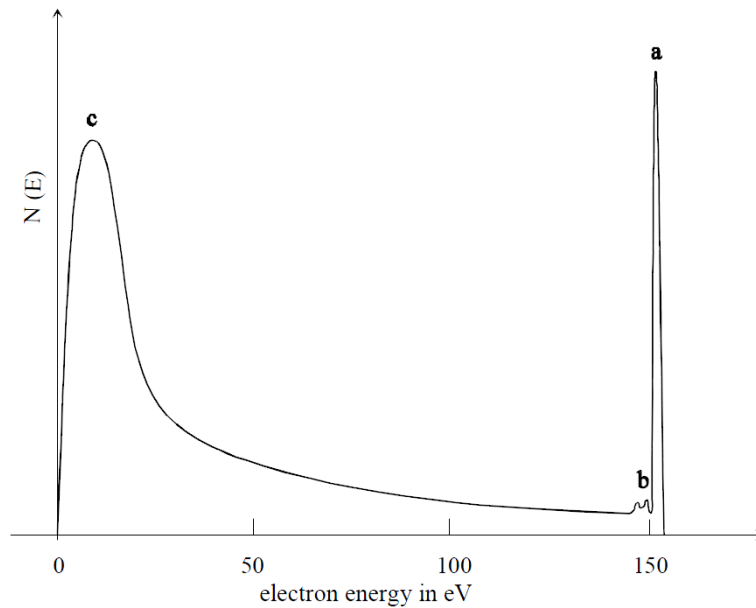


Figure 2.2: Energy distribution of electrons emitted by silver upon bombardment with 155 eV primary electrons, where $N(E)$ is the number of electrons [2].

There are three main groups of secondary electrons that are designated in figure 2.2 and which have to be distinguished:

True secondary electrons are the majority of emitted electrons with low energy around peak c). These electrons derive their origin from the material's electronic structure where they once were bound electrons. Generally, all electrons with an energy below 50 eV are considered as true secondaries. This approximation has to be made because it is impossible to determine the origin of individual electrons.

Inelastically backscattered electrons are located in the range between 50 eV and 150 eV (primary energy). These are also primary electrons which lose some of their energy to the solid surface when impinging. The two smaller peaks at b) are referred to Auger electrons with a discrete amount of energy.

Elastically reflected primary electrons do not encounter any energy loss when impinging on the surface and thus, get reflected while keeping their original primary energy. Peak a) corresponds to these electrons.

2.2.2 Secondary Electron Yield

The secondary electron yield (SEY) is the key parameter when dealing with secondary electron emission. It is defined by equ. 2.6

$$\delta = \frac{i_{sec}}{i_{pri}} \quad (2.6)$$

where δ is the SEY, i_{pri} the primary electron current and i_{sec} the secondary electron current, including backscattered and reflected electrons. Thus, it is also called total SEY. For this work the total SEY is of relevance because the total amount of electrons contribute to disturbing effects on the beam. There are other definitions of the SEY which can be found in literature[3], for example the so called true yield, which does not include backscattered electrons for they do not contribute to secondary electron emission. In the following, always the total SEY is meant.

2.2.3 Amorphous Carbon Coatings

The mitigation technique to be investigated in this work is the application of thin films of amorphous carbon coatings (aC) to the beam chambers. Carbon coatings are generally characterized by a very low SEY. The reason why different materials have different SEY is not fully understood and hence, there is no theory that could predict the necessary material properties in order to achieve a specific SEY. However, there are some known facts, found through experimental investigations [4]:

- Elements with less electrons generally have a lower SEY and a lower work function
- Insulators (e.g. ceramics) have a high SEY. Here, electrons escape from deeper layers
- Beam scrubbed surfaces are covered by more carbon, deposited during plasma formations due to the ionization of residual gas molecules

Due to these facts, carbon was proposed as coating material. Furthermore, it was found that the SEY of the carbon graphite structure is much lower than the SEY of the carbon diamond structure. Thus, the carbon production has to avoid the diamond form and try to produce only graphite. Additionally, graphite is not very reactive, which becomes important when venting the vacuum system. Here, gas molecules recover the surface and increase the SEY. Figure 2.3 shows the total SEY of different types of amorphous carbon coatings (aC) and a stainless steel reference sample. In the SPS the upper SEY threshold desired for an unaffected operation with LHC beams is 1.3. As figure 2.3 shows, carbon coatings with an SEY even below unity could be produced.

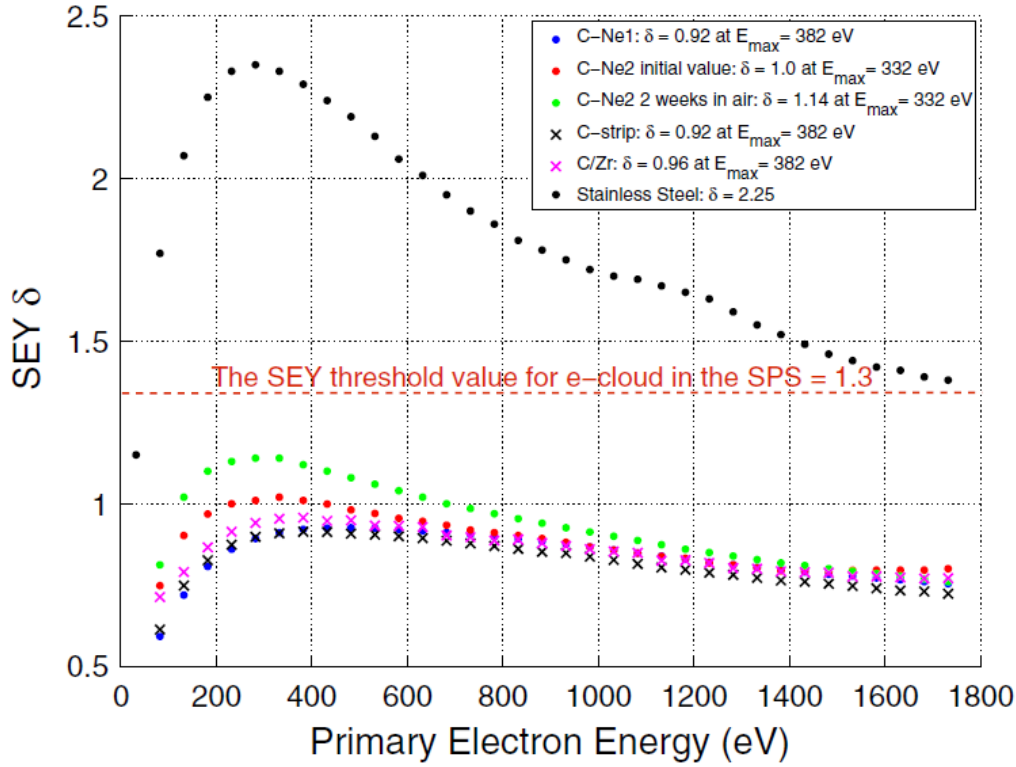


Figure 2.3: Overview of the SEY of aC coatings and stainless steel reference sample. The SEY is also shown as a function of air exposure. The upper threshold value for e-cloud in the SPS operating with LHC beams is 1.3 [5].

2.3 The Multipacting Effect

The expression multipacting (or multipactoring) stems from secondary electron multiplying action. The effect can occur when a time-varying electric field is applied between two opposing surfaces. When accelerated primary electrons impinge on one side, they release secondary electrons. Depending on the kinetic energy, a SEY greater than unity can be achieved. There are two different kinds of multipacting, namely two-surface multipacting and single-surface multipacting.

Firstly, two-surface multipacting is described. When the electric field - in the moment of secondary electron emission - changes direction, the secondary electrons get accelerated to the opposing surface. This releases even more secondary electrons. The effect repeats each half-cycle and accumulates more and more free electrons in the form of an reflecting current which will finally saturate at a certain level. The saturation of the reflecting current is given by the perveance of the gap between the surfaces, meaning that some of the electrons leave the resonant condition with the electric field due to interacting with each other by the Coulomb's force. Sources of primary electrons are, for example, field emission, ionization of residual gas in the vacuum and photo emission due to synchrotron radiation[6].

There is also single-surface multipacting which can occur if a DC magnetic field is applied. The magnetic field can bend the electrons' trajectory in such a way, that they return to the surface they came from, liberating secondary electrons there. This happens then at the end of the second RF cycle, meaning that these electrons were confined in free space during one RF period [7]. In particle accelerators, the

time-varying electric fields are given by the potential of the bunched particle beams. Figure 2.4 shows a scheme of how the electron cloud builds up at the example of an LHC beam pipe. Secondary electrons (green) get attracted and accelerated towards their original surface (single-surface multipacting). Some secondary electrons reach the opposing surface and get reflected or lost (red).

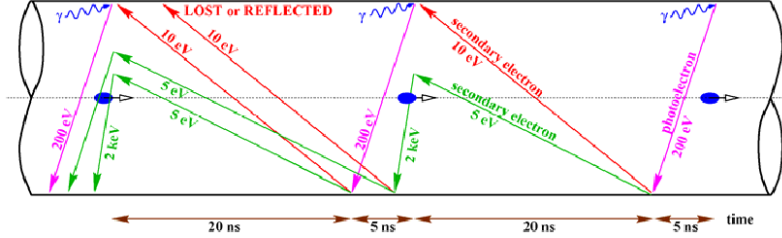


Figure 2.4: Schematic of electron cloud build up in an LHC arc beam pipe, due to photoemission and secondary emission. Secondary electrons get attracted and accelerated by beam potential (green) or reach the opposing surface and get reflected or lost (red) [F. Ruggiero] [8].

Multipacting is also encountered in microwave space applications, especially in satellite communication systems where the implemented RF components are often of a coaxial and waveguide geometry, e.g. waffle-iron type waveguide filters and have to handle very high RF power under vacuum conditions, similar to the ultra-high vacuum in particle accelerators [9]. In satellites, system failure due to an multipacting breakdown is even more complicated because of the lack of maintenance access.

2.4 Other E-Cloud Mitigation Techniques

2.4.1 Clearing Electrodes

As a first possible solution to suppress the electron cloud, clearing electrodes have been installed in several particle accelerators. The principle of clearing electrodes is to apply high, negative or positive potentials (e.g. 500 V) to them in order to repel or attract the electrons and thus prevent the electrons from escaping the chamber wall. This provides a large mean free path for the passing particle beam. The second possibility is to apply a positive potential, which attracts the free electrons. Using positive potentials requires the electrode to draw a current in order to maintain its potential and not being discharged (see also anodes in cathode ray tubes). Using negative electrode potentials practically does not require drawing a current [10]. The effect of high potentials on the particle beam is even more marginal than the effect of gravity and will at the latest be compensated by the quadrupole magnets, re-focusing the beam.

Here, first test showed that already a single negatively charged electrode clearly suppresses the electron cloud. Installing a second electrode, which is located at the opposite side and is equally charged, slight enhancements in electron cloud suppression have been found. Figure 2.5 shows a simulation of the static field pattern using two clearing electrodes with the same polarity in a circular beam chamber.

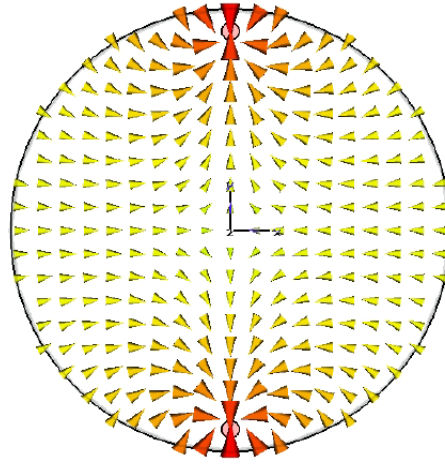


Figure 2.5: Electrostatic simulations of two equally polarized clearing electrodes in a circular beam chamber.[11].

2.4.2 Solenoids

The second possible solution to mitigate the electron cloud is to wrap wires around the beam chamber and feed them with a direct current. Then, the wires generate a solenoidal field, which confines the free electrons close to the chamber walls and thereby limit the electron-beam-interactions and secondary electron emission. This solution has been tested during studies of electron cloud measurements by microwave dispersion in the Low Energy Ring (LER) at Stanford Linear Accelerator Center, where a field of roughly 20 Gauss was generated by the solenoids [12]. Figure 2.6 shows a part of these results, in particular the experimental set-up of these measurements and the measured average electron cloud density versus solenoidal field. These results show a clearly positive effect on electron cloud mitigation, but the solenoids draw a current in order to generate the magnetic field.

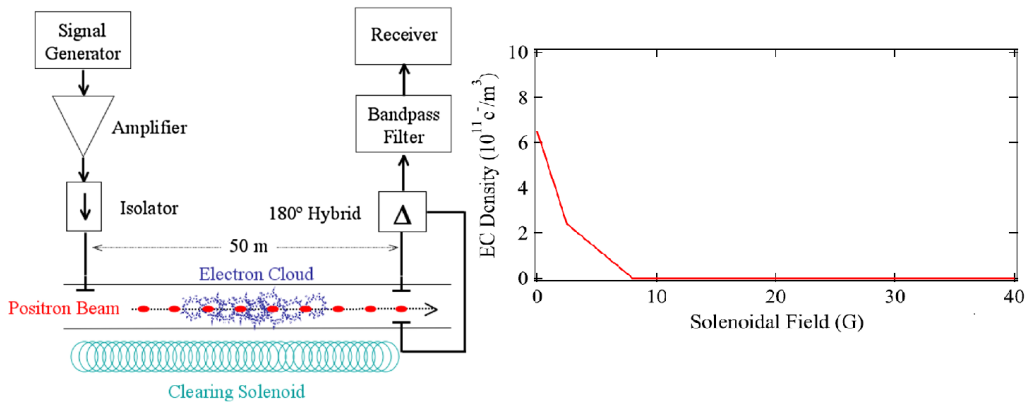


Figure 2.6: Left: Schematic diagram of experimental setup. Right: Average electron cloud density as a function of the beam pipe solenoid field .[12].

2.4.3 Surface Grooves

The effective SEY of a surface can be reduced by increasing its roughness. One way to obtain this effect is to etch grooves on the surface of the beam chamber (see fig. A.1 in the appendix). When a primary electron hits the surface, several secondary

electrons emit with random angles. Depending on the emitting angle, some secondary electrons hit the side walls of the grooves. Most of them are of very low energy (a few eV), meaning that they get absorbed by the grooves. The effect of triangular and rectangular grooves has been studied. Figure 2.7 shows the principle of surface grooves and exemplary trajectories of electrons.

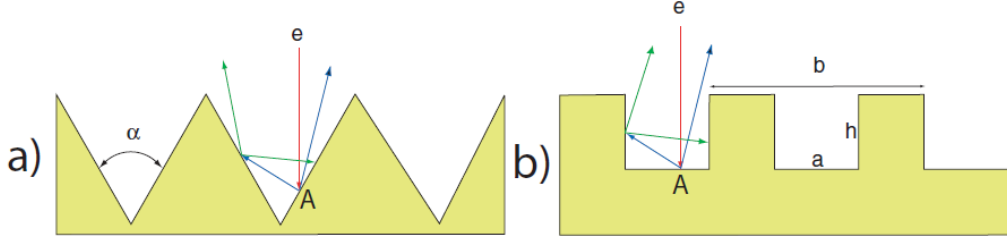


Figure 2.7: Triangular (a) and rectangular (b) grooves on the surface. Triangular grooves are characterized by the angle α . Rectangular grooves have a period b , a dwell width a and a depth h . Red trajectories belong to primary electrons, blue trajectories to first generation secondary electrons and green ones to higher generation secondaries.[13].

For triangular grooves however, there is a mechanism which counteracts the suppression of multipacting. It is due to the fact that the SEY is dependent on the primary electrons' incident angle with respect to the surface normal and typically increases at larger angles. Thus, the first generation secondaries might be larger in number compared to primary electrons impinging on a flat surface. This leaves open some remaining questions on the triangular grooves' efficiency. Simulations show that smaller incident angles with respect to the surface normal generally result in a lower SEY. Further, the simulations yield that the effective SEY does not depend on the size of the grooves but on the angle α .

2.4.4 Advantages of the Carbon Coatings

Considering the alternative mitigation techniques, it is evident that solenoids and clearing electrodes require additional electronic components and, most critical, a lot of space in the magnets and beam chambers. The required space is usually not available. Once applied, the carbon coatings are ideally maintenance-free and practically do not require space nor electronic components. The beneficial effect of surface roughness can also be observed at carbon coatings, which have different grades of roughness, depending on their respective production method.

2.5 Electromagnetic Fields & Relativity

In high energy particle accelerators, the velocity of the charged particles converges to the speed of light. Thus, the principles of Newtonian mechanics are not valid anymore and one has to consider relativistic effects. The correction term for velocities close to the speed of light is given by the Lorentz factor, described in the special theory of relativity. Equ. 2.7 shows the Lorentz factor

$$\gamma = \frac{1}{\sqrt{1 - \frac{v^2}{c^2}}} = \frac{1}{\sqrt{1 - \beta^2}} \quad (2.7)$$

where γ is the Lorentz factor, v the particle's velocity, c the speed of light and $\beta = \frac{v}{c}$. Figure 2.8 shows the electric fields of a static, a slowly moving and a relativistic point charge. As indicated, the electric field for a charge with high β contracts towards the direction of motion. This effect becomes more extreme as the charge approaches the speed of light. Finally, the electric field loses its spherical symmetry but keeps symmetry with respect to the planes which are transversal to the direction of motion. This can be deduced by applying the Lorentz transformation on electric fields [14]. The electric field components in direction of motion become infinitesimal small and thus, are negligible for $v \rightarrow c$.

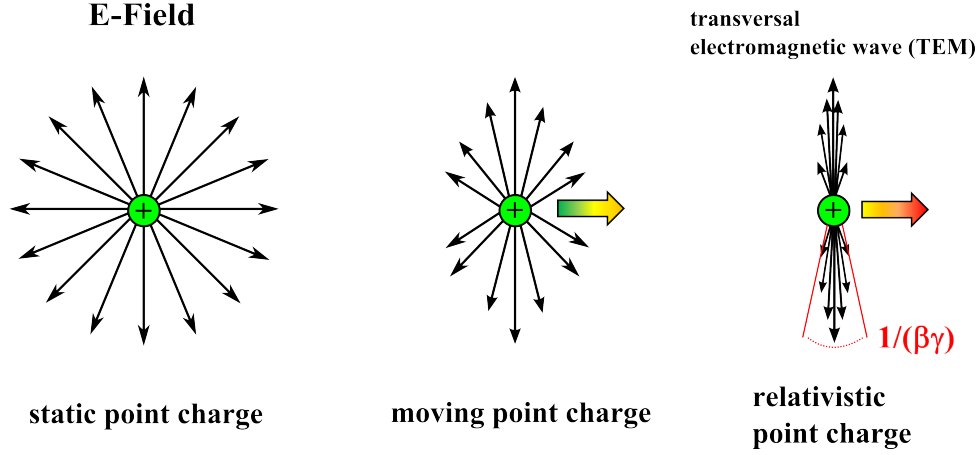


Figure 2.8: Electric fields for a static point charge, a slowly moving point charge and a relativistic point charge (in reality 3-dimensional). For high velocities, the electric field becomes transversal to the direction of motion.

The squeezing angle of the electrical field is given by $\frac{1}{\beta \cdot \gamma}$. This becomes clearer when taking a look to the extreme cases of the static charge ($\beta = 0$) and the relativistic charge ($\beta = 1$). For $\beta = 0$, the angle becomes $\frac{1}{0} \rightarrow \infty$ and thus, expands to a maximum. For the opposite case, where $\beta = 1$, the angle becomes infinitesimal small for γ becomes arbitrarily high, according to equ. 2.7. Then, for the angle it yields $\frac{1}{\infty} \approx 0$. This demonstrates that a highly relativistic particle beam can be approximated by providing a set-up where TEM-Waves can be propagated. This principle underlies the multipacting test stand which will be described later on in this work.

2.6 Modulation Theory

In telecommunications, signal modulation has been used for a long time to encase messages into another signal that can be transmitted, for example modulating a radio frequency signal with a voice signal of lower frequencies for the purpose of radio broadcast. The signal that is modulated and transmitted is usually referred to as continuous wave or carrier wave (CW). In particle accelerators, the electron cloud density can be measured by the magnitude of phase modulation of a carrier wave. The carrier wave encounters the phase shift when passing the plasma. This section provides the basic knowledge of modulation theory, which is used for the in-situ electron cloud diagnostics by means of microwave transmission. It is extracted from [15].

2.6.1 The Carrier Wave

The carrier wave is a pure sinusoidal wave and is given by equ. 2.8.

$$\nu(t) = A \cdot \cos(2\pi f_c t + \varphi) \quad (2.8)$$

where A is the carrier amplitude, f_c the carrier frequency and φ the carrier phase offset. Modulation techniques can be divided into two main categories, *amplitude modulation (AM)* and *angle modulation*. Amplitude modulation means that the amplitude of the carrier wave becomes time-variant instead of being a constant, whereas angle modulation implies that the angle of the cosine term is varied. Angle modulation can be subdivided into *frequency modulation (FM)* and *phase modulation (PM)*. For all modulation techniques and in the frequency domain, the modulation frequencies appear in side-bands which broaden the bandwidth occupied by the carrier.

2.6.2 Amplitude Modulation

An amplitude-modulated signal can be described as shown in equ. 2.9.

$$\nu(t) = A_c[1 + a \cdot m(t)] \cdot \cos(2\pi f_c t) \quad (2.9)$$

where A_c is a constant to determine the overall amplitude, a the modulation index ($0 \leq a \leq 1$), $m(t)$ a normalized modulating signal and f_c the carrier frequency. Figure 2.9 shows a sinusoidal carrier wave, a modulation signal and the amplitude-modulated signal. Eq. 2.9 can be rearranged in a carrier part and a sideband part, yielding

$$\nu(t) = \underbrace{A_c \cdot \cos(2\pi f_c t)}_{\text{carrier}} + \underbrace{A_c \cdot a \cdot m(t) \cdot \cos(2\pi f_c t)}_{\text{sidebands}} \quad (2.10)$$

$$\nu(t) = \nu_c(t) + \nu_s(t) \quad (2.11)$$

where $\nu_c(t) = A_c \cdot \cos(2\pi f_c t)$ and $\nu_s(t) = A_c \cdot a \cdot m(t) \cdot \cos(2\pi f_c t)$. Setting the modulation signal to $m(t) = \cos(2\pi f_m t)$, where f_m is the modulation frequency, and inserting it into equ. 2.10, then

$$\nu(t) = A_c \cdot \cos(2\pi f_c t) + A_c \cdot a \cdot \cos(2\pi f_m t) \cdot \cos(2\pi f_c t) \quad (2.12)$$

Using the relation

$$\cos A \cos B = \frac{1}{2}[\cos(A + B) + \cos(A - B)] \quad (2.13)$$

and apply it to eq. 2.12, it yields

$$\nu(t) = A_c \cdot \cos(2\pi f_c t) + \frac{aA_c}{2} \cdot [\cos(2\pi(f_c + f_m)t) + \cos(2\pi(f_c - f_m)t)] \quad (2.14)$$

Figure 2.9 shows an amplitude-modulated signal in the time domain and fig. 2.10 shows the spectrum of an amplitude-modulated signal with a centered carrier wave at the frequency ω_c and the modulation sidebands at $\omega_c \pm \omega_m$. The amplitude of the sidebands depends on the modulation index a , where $0 \leq a \leq 1$. Thus, the amplitude of the sideband cannot exceed half of the carrier's amplitude.

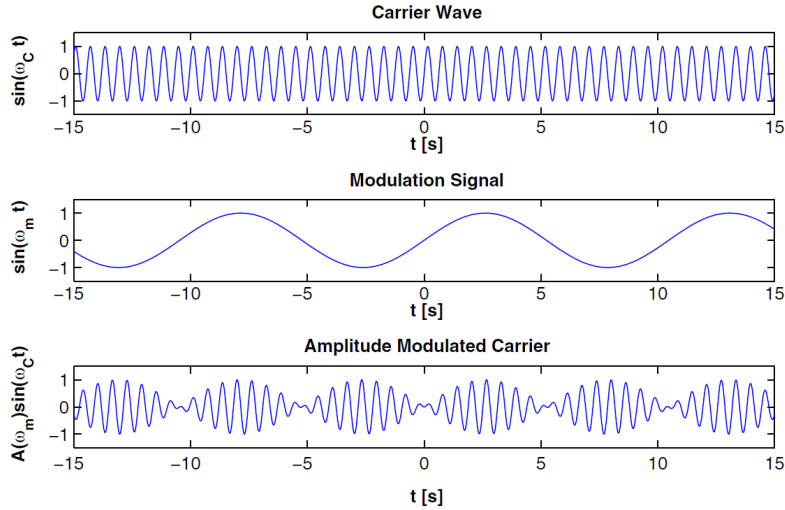


Figure 2.9: Example of an amplitude modulation in the time domain with the carrier wave (top), the modulation signal (center) and the amplitude-modulated signal (bottom) [16].

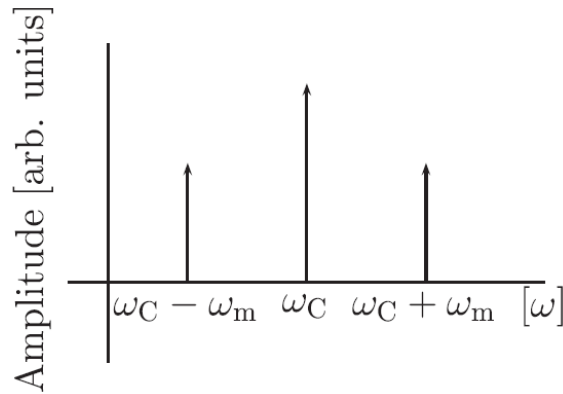


Figure 2.10: Example of an amplitude modulation in the frequency domain with the centered carrier wave at ω_c and the modulation at $\omega_c \pm \omega_m$ [16].

2.6.3 Phase Modulation

Equation 2.15 shows an angle-modulated carrier wave:

$$\nu(t) = A \cdot \cos(2\pi f_c t + \varphi(t)) \quad (2.15)$$

where $\varphi(t)$ is the time-varying phase, which contains the modulation information. For phase modulation in particular, the phase term is directly proportional to the modulation signal, shown in 2.16:

$$\varphi(t) = k_p \cdot m(t) \quad (2.16)$$

where k_p is the deviation constant and $m(t)$ the modulation signal. Thus, the phase-modulated carrier is

$$\nu(t) = A_c \cdot \cos(2\pi f_c t + k_p \cdot m(t)) \quad (2.17)$$

Because the time derivative of phase is frequency, the time-variant phase can be written as

$$\frac{d\varphi}{dt} = k_f \cdot m(t) \quad (2.18)$$

$$\varphi(t) = k_f \int_{t_0}^t m(x) dx + \varphi_0 \quad (2.19)$$

where k_f is the frequency deviation constant and φ_0 the initial phase at $t = 0$. Assuming an initial phase of zero, the frequency-modulated carrier is

$$\nu(t) = A_c \cdot \cos(2\pi f_c t + k_f \int_{t_0}^t m(x) dx) \quad (2.20)$$

It is obvious that integrating the modulation signal in a phase-modulated system is equivalent to a frequency-modulated carrier. Considering the modulation signal

$$m(t) = A_m \cdot \cos(2\pi f_m t) \quad (2.21)$$

the frequency-modulated carrier is

$$\nu(t) = A_c \cdot \cos(2\pi f_c t + k_f A_m \int_{t_0}^t \cos(2\pi f_m x) dx) \quad (2.22)$$

Solving the integral of the modulation signal, one gets

$$\nu(t) = A_c \cdot \cos(2\pi f_c t + \frac{k_f A_m}{2\pi f_m} \sin(2\pi f_m t)) \quad (2.23)$$

or

$$\nu(t) = A_c \cdot \cos(2\pi f_c t + \beta \sin(2\pi f_m t)) \quad (2.24)$$

where $\beta = (k_f A_m)/(2\pi f_m)$. Using the relation $\cos(A+B) = \cos A \cos B - \sin A \sin B$, equ. 2.24 is re-arranged to

$$\nu(t) = A_c \cdot [\cos(2\pi f_c t) \cdot \cos(\beta \sin(2\pi f_m t)) - \sin(2\pi f_c t) \sin(\beta \sin(2\pi f_m t))] \quad (2.25)$$

For small β , equ. 2.25 can be approximated to

$$\nu(t) = A_c \cdot [\cos(2\pi f_c t) - \beta \sin(2\pi f_c t) \sin(2\pi f_m t)] \quad (2.26)$$

and re-arranged to equ. 2.27, using the relation $\sin A \cdot \sin B = \frac{1}{2}[\cos(A-B) - \cos(A+B)]$

$$\nu(t) = A_c \cdot \cos(2\pi f_c t) + \frac{A_c \beta}{2} \cdot [\cos(2\pi(f_c - f_m)t) - \cos(2\pi(f_c + f_m)t)] \quad (2.27)$$

One can see that a frequency-modulated signal is almost identical to an amplitude-modulated signal. The small difference is in the lower sideband, where the phase is shifted 180°. Figure 2.11 and fig. 2.12 show an phase-modulated signal in the time domain and in the frequency domain, respectively.

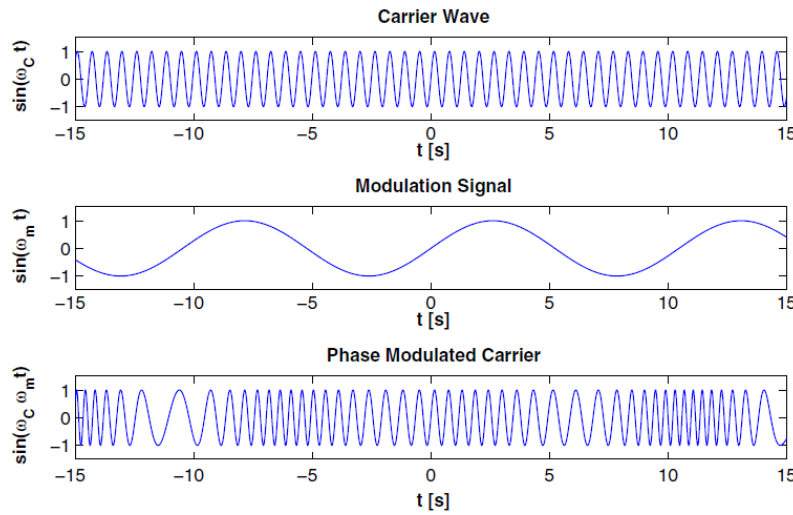


Figure 2.11: Example of an phase modulation in the time domain with the carrier wave (top), the modulation signal (center) and the phase-modulated signal (bottom) [16].

2.6.4 Combined Modulation

In high-frequency circuits different forms of modulation can appear simultaneously. Often, a part of the AM is converted to PM, resulting in a mixture of both modulations in the output signal. In the frequency domain, this conversion causes

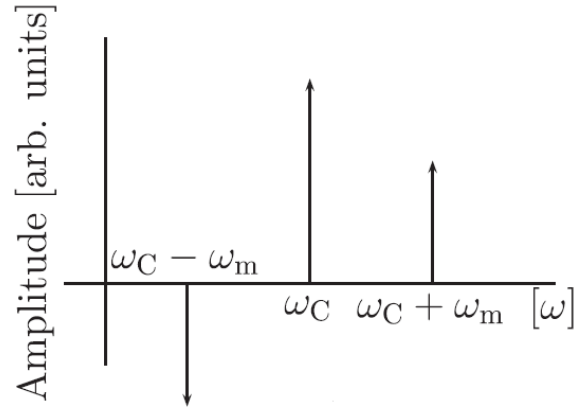


Figure 2.12: Example of an phase modulation in the frequency domain with the centered carrier wave at ω_c and the modulation at $\omega_c \pm \omega_m$ [16].

asymmetrical sidebands or even single sidebands. AM→PM conversion (and vice versa) can happen due to an amplitude-limiting device in the circuit like amplifiers or mixers. There, different amplifications or transmission coefficients for sideband frequencies are the reason for modulation conversion. Fig. 2.13 shows the effects of AM→PM conversion in the frequency domain. The effect of combined modulation can affect measurement quality, because it is difficult to disentangle the origin of different modulation sources.

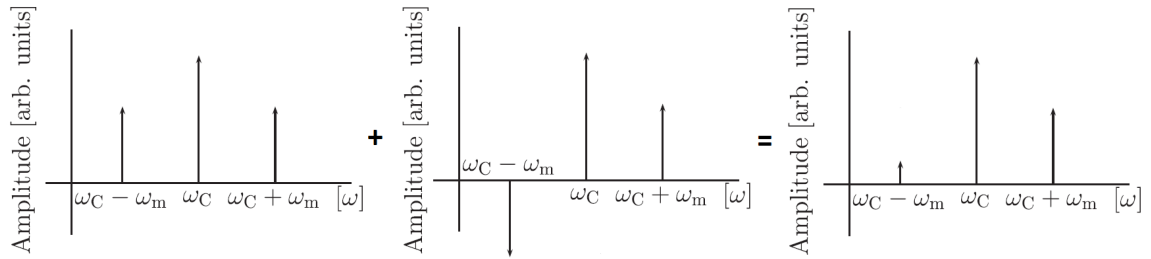


Figure 2.13: AM→PM conversion shown in the spectrum. Different amplifications or transmission coefficients for sideband frequencies can result in a mixture of modulations.

3. The Multipacting Test Stand

3.1 Goal of the Experiment

The multipacting test stand was designed for characterizing uncoated, bare stainless steel SPS beam pipes in terms of their multipacting behavior, as well as to check the effectiveness of multipacting suppression after coating with amorphous carbon. The main goals of this set-up are:

- Induce multipacting in order to see the electron cloud build-up in stand-alone beam chambers (uncoated and coated)
- Find a reliable method which can be used for quality control of carbon coatings, especially in the event of a large scale production
- Make the measurements possible, independent of the real accelerator and particle beam and thus, from the accelerator's schedule
- Provide controllable laboratory conditions

Thus, it was decided to use stand-alone SPS bending magnets and apply the technique of approximating the electric field of a relativistic beam with a coaxial configuration of the electric field as a representative approximation of a relativistic beam of charged particles.

3.2 The experimental Set-Up

The basis of the multipacting test stand is a stand-alone SPS dipole with a length of 6.4 meters. The cross section of the 316LN stainless steel beam chamber, which is installed in the magnet's yoke, is shown in figure 3.1. In order to achieve the ultra high vacuum in the range from a few 10^{-8} mbar (base pressure), to 10^{-4} mbar (maximal dynamic pressure), the system is connected to a mechanical rough pump and a turbomolecular pump.

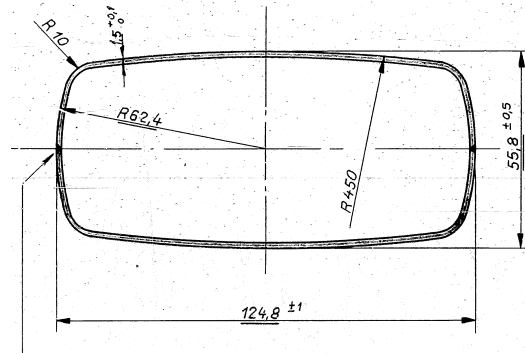


Figure 3.1: Cross section of a MBB-type chamber for SPS bending magnets. Indicated parameters are valid for atmospheric pressure. Length of the chamber is 6.4 meters.

In order to set up a coaxial configuration, a wire with a diameter of 0.5 mm is drawn alongside the beam chamber. The difficulty in this set-up is to draw the wire, center it precisely in the beam pipe and stretch and fix it afterwards. To address these issues, a small pre-chamber has been connected to the front aperture of the beam pipe. The pre-chamber houses a rotatable device for stretching the wire, as well as the electrical transition between the wire and the outer coaxial connector for RF power injection. It also includes the conductances to the pumping system, the vacuum diagnostics and a small viewport to look into the interior of the set-up. Thus, it is a necessary and vital part of the set up. Figure 3.2 shows a picture of the experimental set-up.

The connection between the wire and the coaxial connector consists of a short copper wire, insulated with small ceramic pieces. At the far end of the dipole, the wire is terminated with a short circuit to ground. In combination with the beam pipe, the wire forms a resonant coaxial transmission line where transversal electromagnetic waves (TEM) can propagate. This set-up does not operate in a frequency range where waveguide modes appear.

As RF signal generator, a vector network analyzer (VNA) is used. It is followed by an amplifier with a gain of +50 dB in the frequency range of 30 MHz - 200 MHz. The maximum output power the amplifier can provide is 50 W. Therefore, we rely on the standing wave pattern which forms in the resonating set-up to achieve the necessary electric field strength, enabling us to induce the multipacting.

The amplified wave passes a directional coupler which is important for diagnostic purposes. After the coupler, the wave travels through the low frequency port of a diplexer. The common port is connected to a matching network in order to achieve a critical mode coupling with the resonator. The high frequency port of the diplexer is terminated with the characteristic impedance of the used coaxial cables (50Ω) to avoid unwanted signal reflections when being unused. The diplexer was put into the system to have the possibility for using additional diagnostics on high frequencies if necessary. Figure 3.3 shows a block diagram of the complete experimental set-up like it is used during the electron cloud measurements.

For the wire material, tungsten has been chosen for its excellent thermal properties. It has the highest melting point of all pure metals and a very low thermal expansion

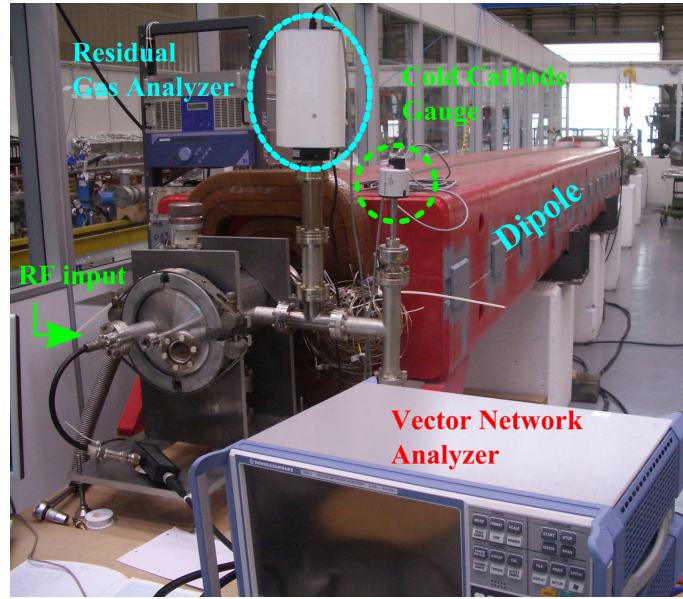


Figure 3.2: Experimental multipacting test stand with the pre-chamber (attached to the SPS dipole), vacuum diagnostics and part of the electronics.

coefficient. This is important to keep the resonant frequencies of the system stable and to significantly reduce the danger of damaging the vacuum system or compromising the quality of the ultra high vacuum due to a melt-down of the wire when injecting RF power. Copper as material for the wire would be too soft and collapse under its own weight once it is heated up, especially when considering the length of the dipole (6.4 meters). However, the increased stability using tungsten is traded off for a much lower Q-factor than with copper due to its much lower conductivity. This means that an important part of the energy is dissipated in the tungsten wire instead of being stored in the resonator in form of a larger electromagnetic field.

3.3 Diagnostic Methods

In order to detect the multipacting effect and the subsequent electron cloud presence, the experiment uses vacuum diagnostics as well as diagnostics by means of RF-plasma-interaction. For vacuum diagnostics, a compact cold cathode gauge and a Prisma QMS200 residual gas analyzer are connected to the vacuum system. A process ion gauge can be used to monitor the pump down during the first few minutes when the pressure is still too high and might damage the cold cathode gauge (Penning gauge). Later on, it is switched to the cold cathode gauge which is sensitive in the ultra low pressure range. The Prisma QMS200 is used to observe the composition of the system's residual gas, especially the dynamic rise of the different gas species during the multipacting event, caused by electron-stimulated desorption.

The RF diagnostic relies on the VNA. Due to the presence of the electron cloud plasma, some of the RF input power gets reflected. Electrons get accelerated by the electric fields and thus, radiate because the acceleration vector is changing. In addition, the plasma formation causes a slight change in impedance, resulting in smaller, local resonances which reflects input power. However, reflections due to a change in impedance are very small in this case and thus, negligible. All reflected power that leaves the resonator will be coupled out by the directional coupler and

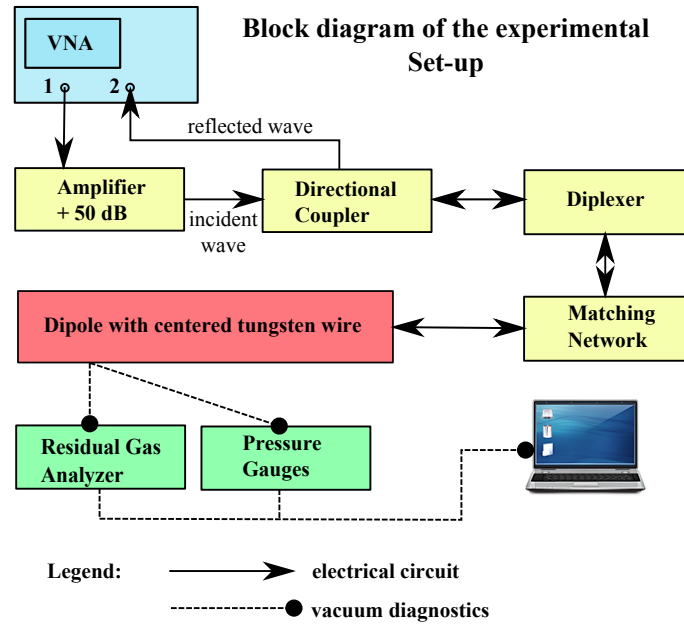


Figure 3.3: Block diagram of the experimental set-up. Electrical circuit and power diagnostics (beige), dipole (red) and vacuum diagnostics (green) are shown.

sent to the second port of the network analyzer. There it will be compared to the VNA output power. Considering the network analyzer as both, signal generator and diagnostic tool, as well as the amplifier, one has created some sort of **high power network analyzer**. Its principle of operation is explained in the following section in greater detail.

3.4 Analysis of the electrical Circuit

As it was mentioned above, the reflected power is measured in order to characterize the multipacting behavior and electron cloud build-up. Although only the power reflected by the electron cloud is of interest, the VNA additionally receives undesired reflected power from other sources along the electrical circuit, which unfortunately contribute to the total measurement signal. The main source of undesired reflection in this set-up usually is a slight mismatch in the matching network before the power enters the resonator. This part of the power does not only get reflected and contributes to the measurement signal, but it is lacking in the resonator, resulting in lower field strengths to induce the multipacting. Therefore, it is necessary to get as close as possible to critical mode coupling in order to reduce these reflections to a minimum.

For each resonant frequency the matching network has to be adjusted individually. Figure 3.4 shows the resonances matched for 148.74 MHz. The matching network consists of a T-junction in the transmission line towards the resonator and was tuned by coaxial cables with different lengths, connected to the third port of the junction. Because the lengths of cables are standardized, it was not always possible to get a clean critical coupling and thus, the coupling was always slightly over- or undercritical.

Taking a look at the equidistant resonances, it is evident that the fundamental mode in the dipole is excited at ≈ 20 MHz. This can also be calculated, given the speed

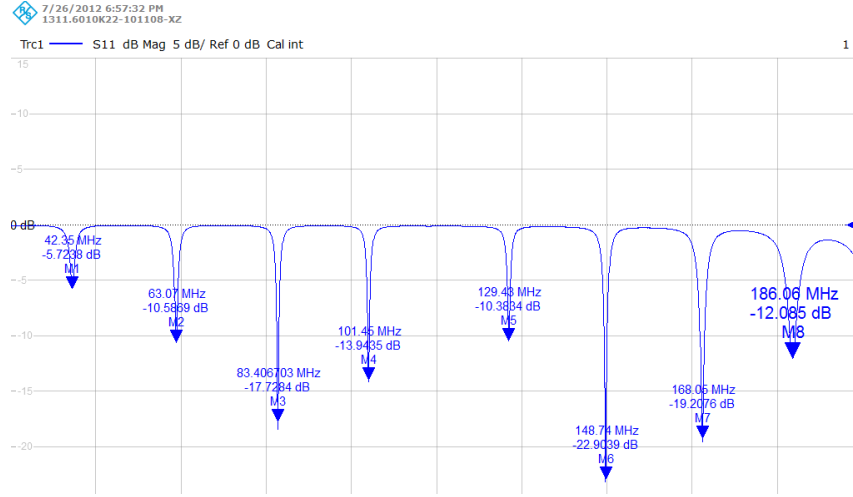


Figure 3.4: Resonances of the matched resonator. The resonant frequency at 148.74 MHz is matched best in this case.

of light ($3 \cdot 10^8$ m/s) and the length of the dipole (6.4 m) and assuming, that $\lambda/2$ is the first standing wave fitting in the resonator. The calculation with the given parameters yields

$$f_{\lambda/2} = \frac{3 \cdot 10^8 \text{ m/s}}{2 \cdot 6.4 \text{ m}} = 23.43 \text{ MHz} \quad (3.1)$$

which shows very good agreement to the measured values. The discrepancy in the calculated frequency is due to the fact that the real resonator is not only the dipole but also the connected pre-chamber which is part of the resonating coaxial configuration.

In order to separate the returning power waves from the incident waves, a directional coupler was inserted in the circuit. Directional couplers have several key parameters which are listed below:

Directivity indicates the power ratio between the forwarded power and the power that is unintentionally coupled out through the reflection branch despite the proper termination of the main branch. Clearly, this ratio should be as high as possible.

Coupling factors describe which part of the power (forward and reflected) is coupled out through their respective coupling ports.

Insertion loss is the loss of power after passing the main branch. Hereby, ohmic losses and losses due to coupling are considered.

Voltage Standing Wave Ratio (VSWR) is the ratio in amplitude of a maximum and a minimum in a partially standing wave and thus, related to the reflection coefficient. A VSWR of 1:1 means that both half waves are equal in amplitude and the wave is undisturbed by occurring reflections.

The directional coupler that has been used throughout all performed measurements so far, is in fact a dual directional coupler, providing the double amount of coupling ports. Therefore, it is important to terminate all unused ports with the characteristic impedance of $50\ \Omega$ in order to avoid undesired reflections. The coupler's parameters are a directivity $> 30\ \text{dB}$, a coupling factor of $30\ \text{dB}$ and a VSWR of 1.05:1. Figure 3.5 shows a picture of the coupler.

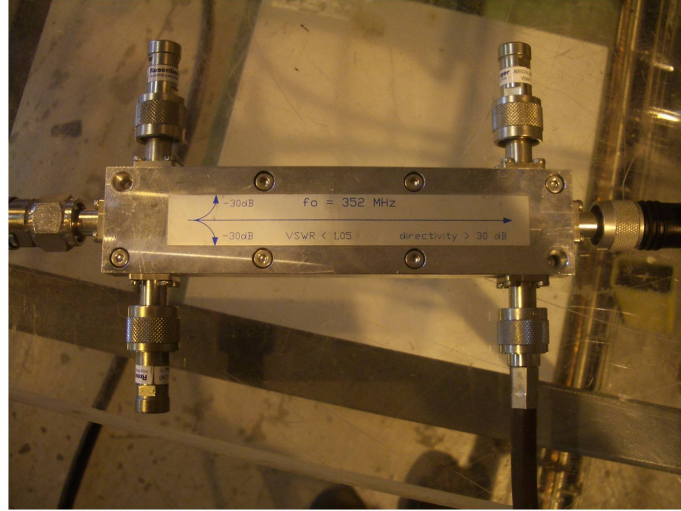


Figure 3.5: Dual Directional Coupler and its parameters.

As it is denoted in the picture, the center frequency, in whose vicinity the $30\ \text{dB}$ coupling factor is assured, lies at $352\ \text{MHz}$ which is above the set-up's operating frequency range of $30\ \text{MHz} - 200\ \text{MHz}$, limited by the amplifier. Figure 3.6 shows the transmission measurement of the coupling port for the reflected power. It can be clearly seen that the coupling factor decreases for lower frequencies. This has to be taken into account when extracting quantitative power information, especially when performing the multipactor tests on different resonant frequencies. Unfortunately, no other coupler was available at that time.

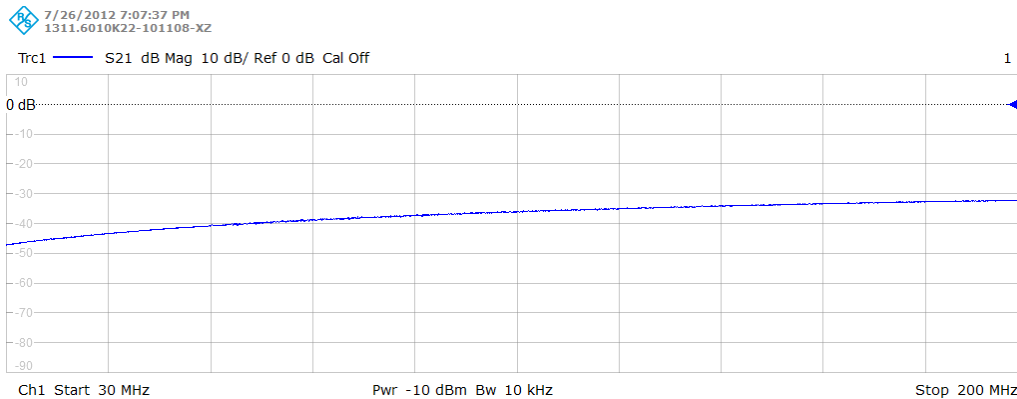


Figure 3.6: Transmission measurement of the coupling port for the reflected power in the operating frequency range. The coupling factor decreases with lower frequencies.

The electric circuit also contains a diplexer, where the transmission line is divided into a low-frequency line with the range from basically zero to $1.5\ \text{GHz}$ and a high-frequency line with the range from $1.75\ \text{GHz}$ to $2.4\ \text{GHz}$. The low-frequency line is

connected to the wire in the test stand, because the operating frequencies belong to the low-frequency range with respect to the coupler's transmission properties. The high-frequency port usually was terminated with the characteristic impedance, but may be used for additional diagnostics on high frequencies in the future. Figure 3.7 shows the transmission properties of the diplexer for both, low-frequency and high-frequency range.

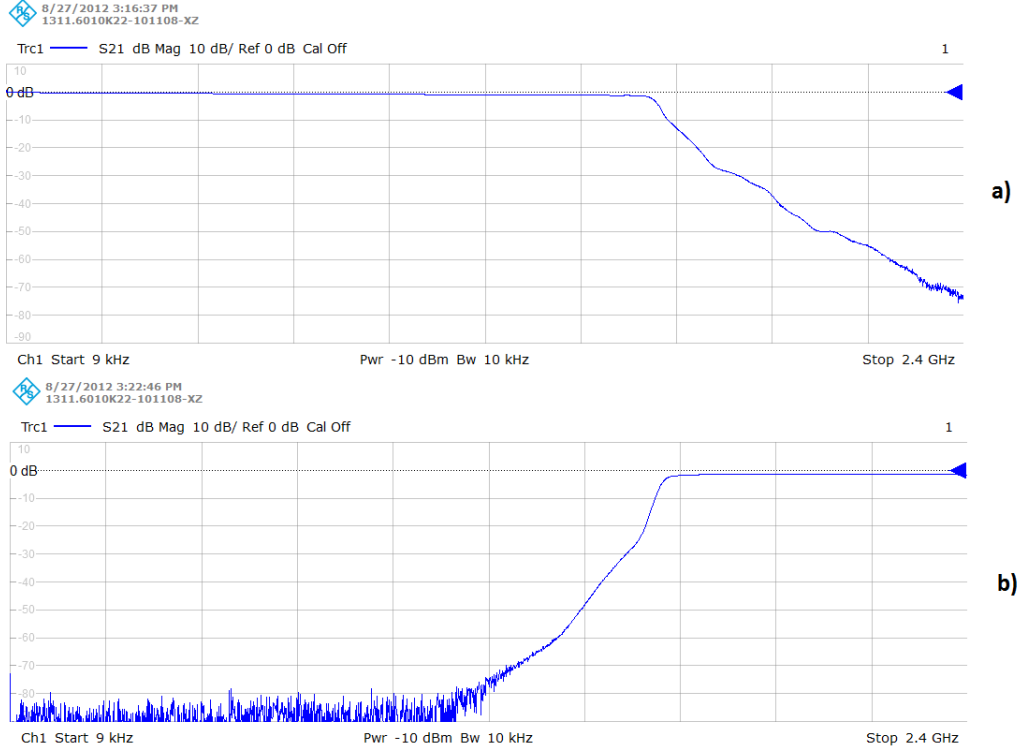


Figure 3.7: Transmission properties of the diplexer for a) low-frequency range and b) high-frequency range.

3.5 Commissioning of the Set-up

3.5.1 Pump down and Leak Detection

When all flanges are properly closed the pumping system can be started and the decrease in pressure has to be monitored. In the case of a vacuum leak in the system, the pressure becomes static at a relatively high level, very early in the pumping process. In order to detect the location of leaks, the residual gas analyzer can be used under the condition, that the pressure is below 10^{-4} mbar. For leak detection, the RGA is set to scan the vacuum for helium-4, which has to be injected at any crucial connections where leaks are suspected. Note, that if the signal in helium is strongly delayed it is an indication that the gas could have entered the system through the back of the pumping system. In the case that no leak is present, the helium-4 signal does not increase.

3.5.2 Wire Fault Detection via Time Domain Reflectometry

Once all flanges are closed and the system is pumped down, there is no possibility to check the wire's stretching and proper termination in a visible way. However, with

the vector network analyzer, it is possible to perform a time domain reflectometry (TDR) which indicates the reflection coefficient over time. Thus, it is possible to detect any discontinuity in the transmission line.

To perform the TDR, the network analyzer is set to measure the reflection coefficient (S11). During this procedure, the VNA is directly connected to the resonator for it is necessary to have an impedance mismatch to see the wire. Considering a homogeneous wave propagation, the reflection coefficient is also given over the length of the wire [17].

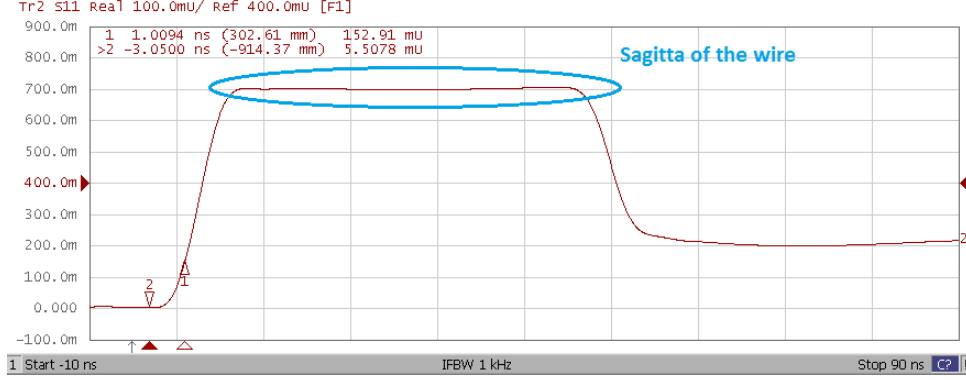


Figure 3.8: TDR measurement of the stretched wire. Reflection coefficient vs. time (and length) is displayed. The reflection coefficient strongly increases at the transition between the 50Ω impedance of the electronics and the wire. If the wire is well stretched, it remains stable (plateau) until it decreases due to the short circuit termination.

Figure 3.8 shows the reflection coefficient of a well stretched wire. As excitation signal the step function is used. Also the shape of the wire and its sagitta is visible. The reflection coefficient results from the difference in impedance between the coaxial cables and the resonator. Using the equation for the reflection coefficient, one can calculate the impedance of the wire:

$$\Gamma = \frac{Z_{wire} - Z_0}{Z_{wire} + Z_0}. \quad (3.2)$$

where Z_{wire} is the impedance of the wire, Z_0 the characteristic impedance of the measurement system (50Ω) and Γ the reflection coefficient, given by the measurement.

Solving the equation for Z_{wire} , one gets

$$Z_{wire} = -\frac{(\Gamma + 1) \cdot Z_0}{\Gamma - 1} \quad (3.3)$$

For $\Gamma = 0.7$, the impedance of the wire can be calculated to 283.3Ω . Looking at the length of time of the plateau, it shows about 50 ns. Multiplied with the speed of light, it yields 15 meters. Considering, that the signals have to travel the distance two times, the wire is about 7 meters long, which agrees to the length of the dipole (6.4 meters) and the pre-chamber and pumping port (ca. 50 cm).

One would expect that with a short-circuited termination, Γ reduces to -1. The short circuit, however, is non-idealistic and thus, causes secondary reflections in the resonator, superimposing the previous signals. This results in a stepwise reduction of the measured reflection coefficient. Figure 3.9 shows the long term evolution of the reflection coefficient.

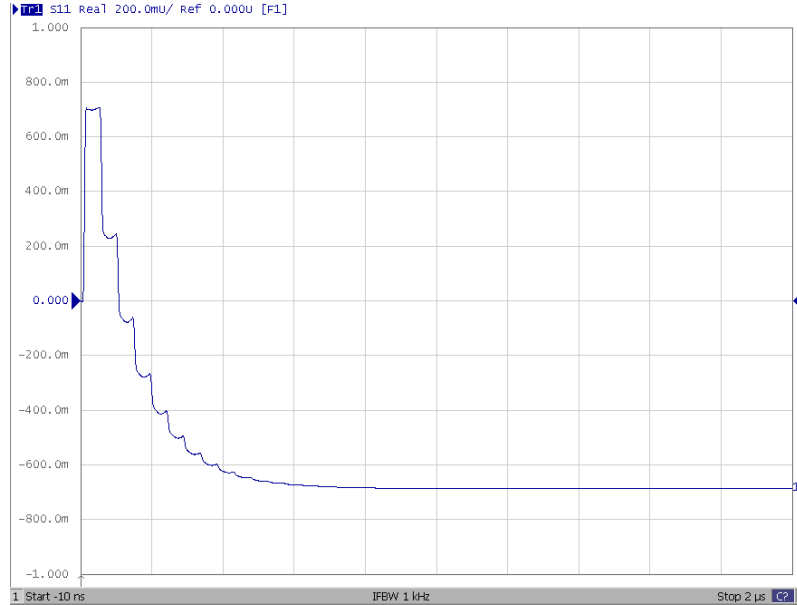


Figure 3.9: Long term evolution of the reflection coefficient of the short-circuited resonator. The short circuited termination is not perfect and thus, causes multiple secondary reflections, traveling forward and backward along the resonator, superimposing the previous signals. This results in a stepwise reduction of the measured reflection coefficient.

3.5.3 Resonant Frequency Identification

Before injecting RF power on a continuous wave frequency, one must identify the resonant frequencies of the system. The resonant frequency depends on the geometry of the resonator. For the identification, the set-up shown in figure 3.3 is necessary because the amplifier and additional electronic devices have to be taken into account. The network analyzer was set to a linear frequency sweep in the range of 30 MHz up to 200 MHz which are the frequency limits of the amplifier. The output power of the network analyzer was set to -30 dBm ($1 \mu W$). Remembering the 50 dB gain of the amplifier, this low output power prevents damage to the VNA and unnecessary power dissipation in the wire which might lead to a resonant shift due to its thermal expansion.

Once the resonant frequencies are identified, they must be used as continuous wave frequency (CW frequency) for power injection when performing the actual experiment. In order to fully understand the received differences, one has to know how the signal is produced:

The VNA compares the incoming wave to the emitted wave. Thus, the magnitude cannot exceed 0 dB in conventional use. But since the amplifier is intercalated in the final measurement set-up, the values in magnitude are shifted higher, because the VNA is not aware of the amplifier. Figure 3.10 shows the difference between

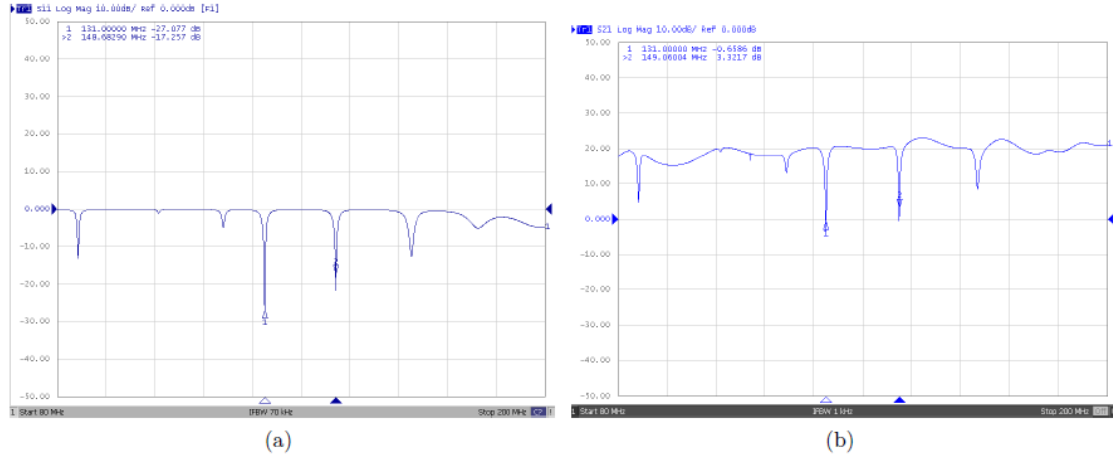


Figure 3.10: (a) resonant frequencies in conventional use of the VNA and (b) with an intercalated amplifier.

conventional measurements and measurements with an intercalated amplifier [18]. The bumps on the top of the signal are related to the gain variation over frequency range (gain flatness).

3.5.4 Dipole Transfer Function

For performing measurements with different magnetic fields, one has to know the correlation between applied DC current in the dipole and the corresponding magnetic field it produces. Therefore, a transfer function is necessary that allocates currents to magnetic fields. This is important to calculate, which current has to be applied to the magnet in order to generate the magnetic field, matching the cyclotron resonance for a given injection frequency. Figure 3.11 shows the transfer function of a reference dipole.

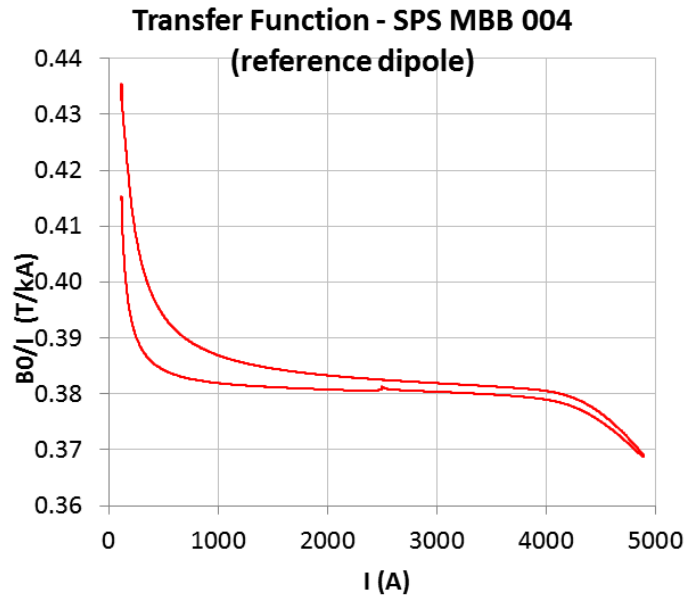


Figure 3.11: Transfer function of a reference dipole with small non-linearities at its extremities.

3.5.5 DC Current Heating

Due to several concerns about how much multipacting can occur on the wire's surface in addition to the chamber walls, it has been tested to heat the wire by feeding with a low DC current over certain time. Therefore, a DC power supply was connected to the inner conductor of the N-type coaxial connector at the RF power input (direct connection to the wire). It was assured that the far end of the wire was properly short-circuited so that a DC current could be applied. The wire has been heated up for 90 minutes at 5 V and 1 A. During this test a lot of thermal desorption could be observed. The recordings from the residual gas analyzer are shown in fig. 3.12

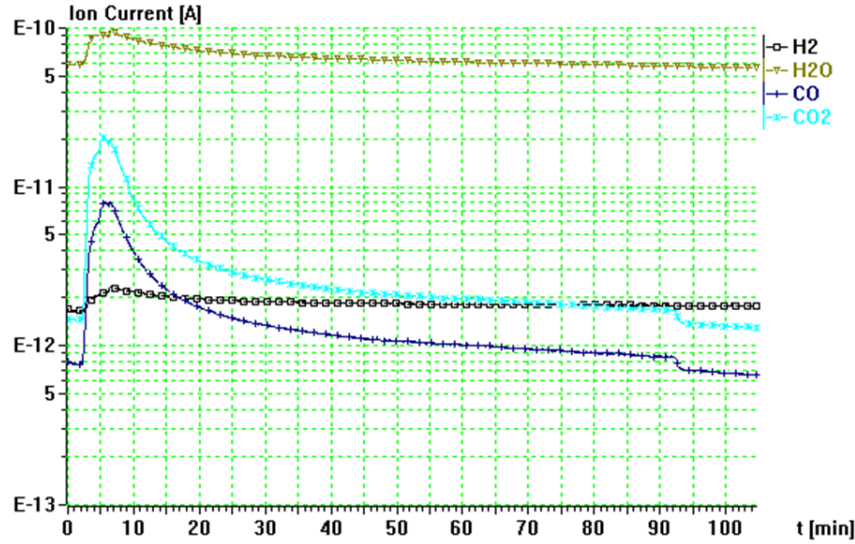


Figure 3.12: Thermal outgassing during heating with a DC current. The slow reduction of the signals and the fact that water remains the dominant species in the system is characteristic for thermally induced outgassing.

No beneficial effect could be observed in the following measurements. On the contrary, it took a very long time for the wire to cool down until the resonances were stable again and the next measurements could take place. The wire's cooldown is additionally delayed due to the fact, that there is no convection in the ultra-high vacuum and the wire can only lose its heat by irradiating.

3.6 Simulations

3.6.1 ESA-ESTEC Multipactor Calculator

The ESA-ESTEC Multipactor Calculator was programmed to support the design and testing of margin values in terms of RF multipacting breakdown for European space missions. Detailed information can be found in the standard ECSS-E-20-01A [19] by the European Corporation of Space Standardization (ECSS). Because the present problems of multipacting in particle accelerators are underlain by the same principle and similar conditions, it is possible to use this software in order to estimate the power threshold of the multipacting onset for a given waveguide configuration.

A first simulation has been performed for the resonant frequency of 130 MHz which was found during the commissioning of the set-up. Because the options of this software are quite limited, the SPS chamber was herein approximated by a square-coaxial transmission line. For the inner conductor, the 0.5 mm diameter of the wire

was entered. For the outer conductor, the smaller diameter of the rectangular SPS chamber (55.8 mm) has been entered because the electric field strength is much higher in the vertical plane than in the horizontal plane. The materials in the software are predefined. Thus, copper has been chosen for it is closest to the SEY of stainless steel. Figure 3.13 shows the results, calculated by the simulation software.

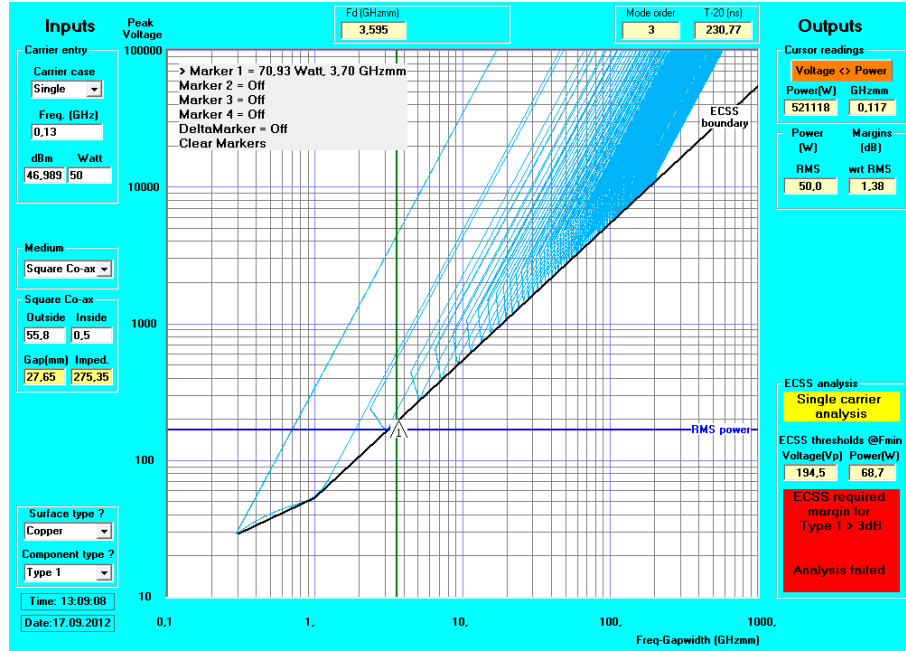


Figure 3.13: ESA Multipactor Calculator simulations with the dimensions of the SPS chamber and the resonant frequency of 130 MHz.

The simulation shows voltage (or power) versus the frequency-gap-product (fd -product), which is defined by the carrier frequency and the dimensions of the waveguide. The fd -product is represented by a vertical green line. The power threshold for the multipacting onset is determined by the intersection point of the fd -product and the ECSS boundary which is represented by the thick black line. Taking a look at the cursor readings, the power threshold for the multipacting in this configuration is 71 Watt. However, this simulation tool considers traveling waves. The multipacting test stand, however, uses standing wave. Because the peak voltage doubles at the maxima, the calculated power threshold has to be divided by four, remembering that power is proportional to the voltage squared. Thus, the power threshold should be expected about 18 Watt continuous wave power to induce multipacting in the experimental set-up.

A second simulation has been performed at 68 MHz, which is also a resonant frequency of the experimental set-up (see fig. 3.14). The results yield a power threshold of about 4 Watt (already divided by four). This means generally that for lower frequencies the necessary power to induce the multipacting drops. This is not surprising if one considers that at higher frequencies the free electrons also need to be more accelerated in order to reach the opposing surface within one half-cycle and subsequently to maintain a resonant secondary electron emission.

Additionally, this simulation tool also provides a calculation of wave impedance. The wave impedance for the used waveguide parameters is given with 275.35Ω , which is in good agreement with the TDR measurement results of 283.3Ω (see section 3.5.2).

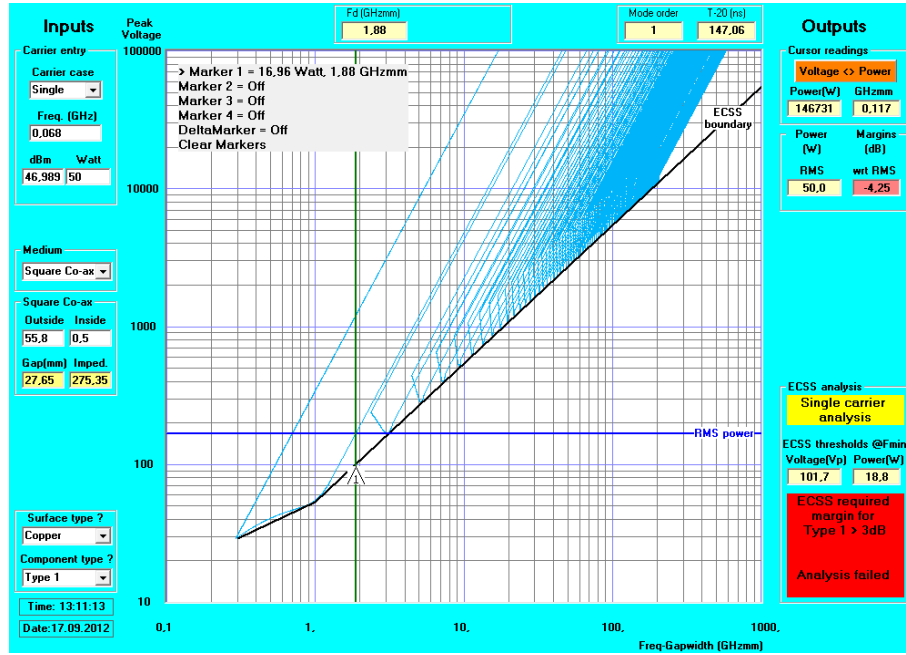


Figure 3.14: ESA Multipactor Calculator simulations with the dimensions of the SPS chamber and the resonant frequency of 68 MHz.

3.6.2 CST Microwave/Particle Studio

The SPS beam chamber was modelled in CST Microwave/Particle Studio, where the electromagnetic field distribution can be simulated and particle emission and growth can be tracked, depending on SEY-curves of the used material (credits to Luca Ficcadenti). The resonating frequencies are yielded by the implemented Eigenmode-solver. One of these frequencies is 131.03 MHz, which also has been measured in the real set-up. This mode is considered in all following simulation results. Figure 3.15 shows one half of the modelled SPS chamber with a centered wire and emitted particles after one RF period (left) and after many RF periods (right). The initial number of electrons is 1500, homogeneously distributed on the surface of the wire, which is the emitting surface. The initial energy was set to 4 keV. These simulations follow the probability model of M.A. Furman [20].

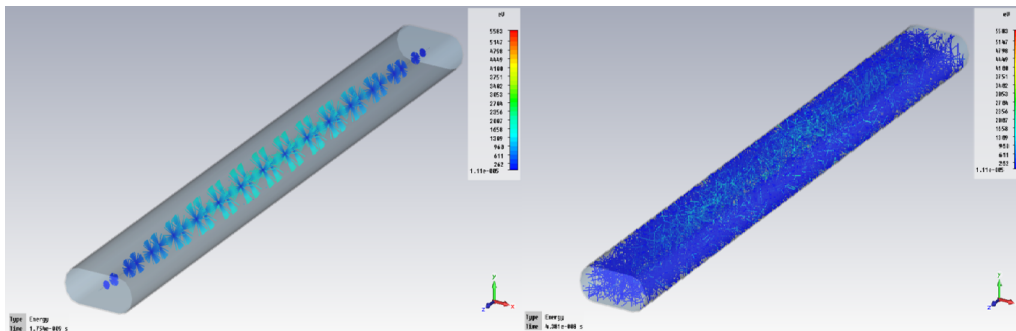


Figure 3.15: Particles after one RF period ($\lambda/2$) at 1.75 ns (left) and after several RF periods at 43.8 ns (right).

Magnifying the model shows, that several secondary electrons with lower energy get emitted from the chamber's surface. They are depicted in figure 3.16, indicated by red circles.

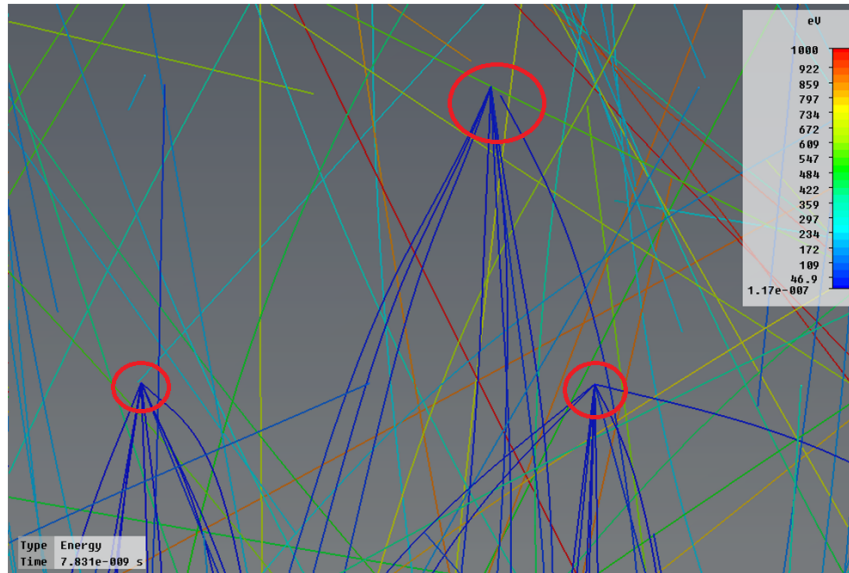


Figure 3.16: Low energy secondary electrons, emitted by the chamber wall (red circles). Electron energy is indicated by color from low (blue) to high (red) energies.

Two of the key parameters of these simulations are the maximum emitted electrons per hit and the maximum number of generations. The obtained results depend strongly on these two parameters. Worst-case simulations with maximum 10 emitted electrons per hit and a maximum generation of 20, a clear highly pronounced electron activity is observed at about 20 Watt input power, manifesting in a strongly increasing growth rate of free electrons (see in figure 3.17). The growth rate corresponds to the SEY-curve and is considerably higher for this input power, which is directly related to the electrons' energy. The growth rate saturates at a certain point, which is due to the fact that electrons with very high energy are more likely reflected instead of liberating secondary electrons. These simulations consider the SEY of stainless steel, pre-defined by the simulation tool, and could be optimized in the future by applying measured SEY values of the real stainless steel chamber (and also carbon coatings) for a crosscheck with actual measurement results.

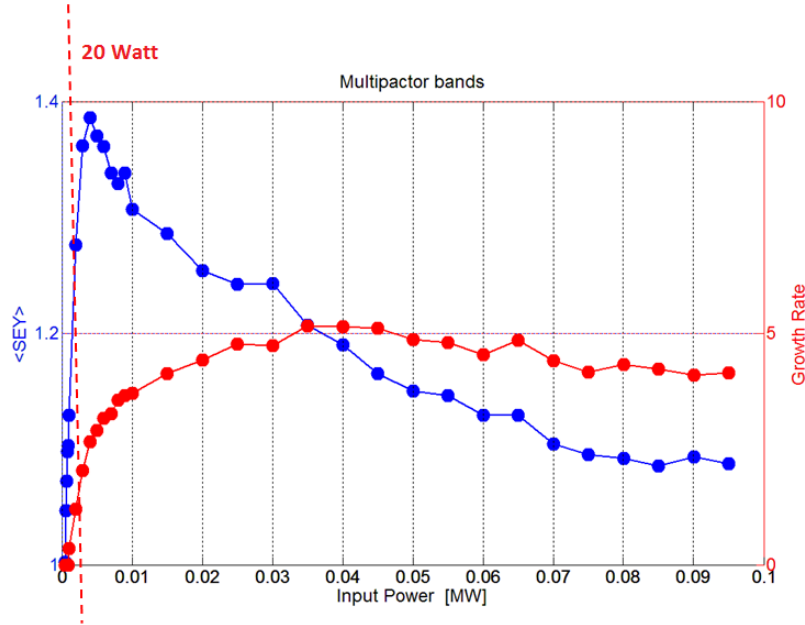


Figure 3.17: The secondary electron yield of the pre-defined stainless steel (blue line) and the particle growth rate (red line) versus input power. A significant electron activity starts at 20 W input power, shown by the strongly increasing particle growth rate.

3.7 Results of the DC cylindrical Magnetron sputtered Coating

This section describes the measurement results of the DC cylindrical magnetron sputtered coating (DCCMS) [21]. For DCCMS, the magnet has to be dismounted and the beam chamber extracted. Firstly, it is dealt with a general characterization of the bare stainless steel chamber in order to collect reference data. Secondly, the measurement results of the coated chamber are shown and discussed. The results of this coating were also published and presented at IPAC'12 [22].

3.7.1 Characterization of the Stainless Steel Chamber

The measurements were performed with RF frequencies of around 130 MHz which is one of the resonances given by the chamber's geometry. This frequency was chosen, because it was matched best without applying an additional matching network. A power sweep from -30 dBm to -8 dBm over 5 seconds on the network analyzer - linear in logarithmic scale - was performed on this frequency to induce the multipacting. This resulted in a maximum output power by the amplifier of about 30 W. The measurements were performed as a function of magnetic field. Between the measurements there is a pause of around one minute in order to stabilize the wire's temperature. Figure 3.18 shows the reflected RF power of the bare stainless steel chamber for low dipole currents from 4 A up to 200 A (1.76 mT to 88 mT) in the chronological order from low to high currents. Below 4 A, no multipacting could be observed during these measurements.

A closer look to the power diagnostics shows small modulations which can easily be seen before the power levels rose exponentially. It turned out that these modulations

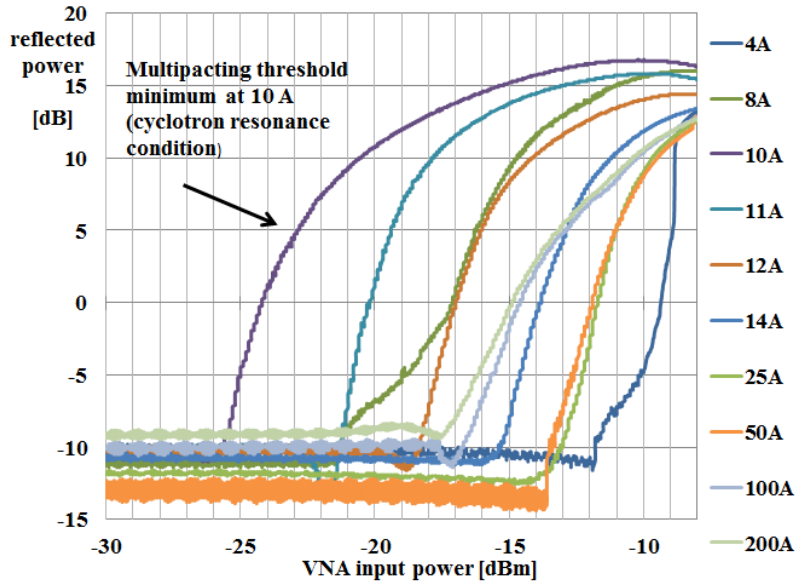


Figure 3.18: Reflected power, measured in the low magnetic field regime on the uncoated chamber. The pronounced line corresponds to the reflected power with 10A, which is the necessary current to achieve the magnetic field of cyclotron resonance for the used frequency.

are caused by the mechanical vibrations of the pumping system which results finally in a vibration of the wire. The change in impedance is caused by the variation of the distance between the wire and the chamber wall which acts as outer conductor of the coaxial-like structure. Thus, it can be seen as a time-dependent asymmetric coaxial transmission line. The base level of the reflexion depends mainly on the mode coupling and other undesired resonances in the electrical circuit.

A pronounced signal in reflected power, gas desorption and pressure rise at cyclotron resonance condition has been observed. During the cyclotron resonance condition a glow discharge in the blue visible (and possibly ultra-violet) spectrum could be observed through the small view port. Figure 3.19 shows the plasma caused by electron multipacting and the subsequent ionization of residual gas molecules. With ongoing measurements the plasma was observed getting weaker and weaker. This is related to the conditioning of the system for there is less residual gas that can be ionized. Unfortunately, the plasma was too weak to apply an optical spectroscopy, with the optical spectrometer available.

In the residual gas analysis, the effect of cyclotron resonance is confirmed and shows a very good agreement to the measured reflected power. Figure 3.20 shows the desorption of hydrogen, water and carbon monoxide molecules for each individual measurement for certain magnetic fields. The mentioned gas species are the mainly desorbed ones which makes them representative. In static conditions, water usually contributes most to the residual gas composition. The fact that, during the pressure burst, H_2O does not exhibit a significant rise but CO and H_2 does is a clear fingerprint of particle-stimulated desorption compared to the mostly thermal outgassing of water due to the heat up of the tungsten wire.

After the characterization with low magnetic fields, the tests were continued using higher magnetic fields. These tests were done to check whether there is a change in

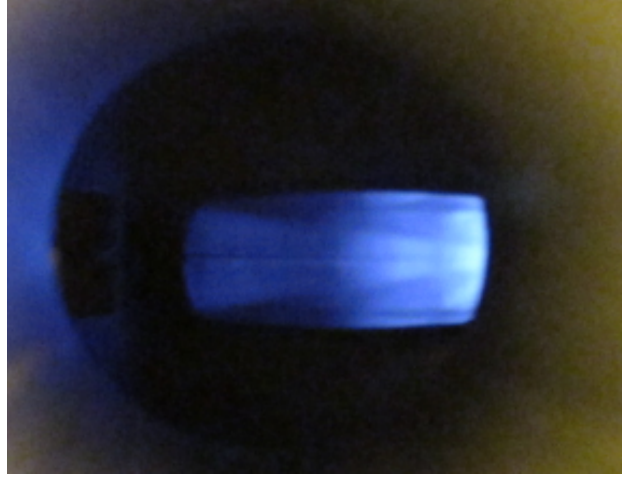


Figure 3.19: Evidence of plasma formation by emitted light in the blue visible spectrum.

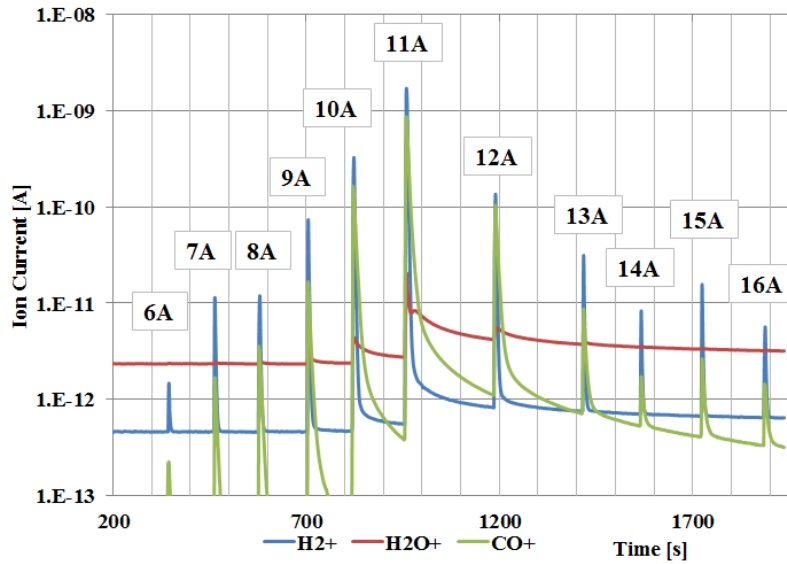


Figure 3.20: Outgassing for hydrogen, water and carbon monoxide at different magnetic fields with a pronounced maximum around the calculated resonant condition (ca. 11 A). The labels on top of the spikes correspond to the current, passing the dipole's solenoids.

the multipacting behavior due to the electron confinement along the magnetic field lines or not. For experiments at very high magnetic fields, the magnet needs to be fed by a large power converter in a special test bench, which also provides water cooling. Thus, measurement time with high currents can be very limited. Figure 3.21 shows the corresponding results. The indicated currents cover a magnetic field range from 380 mT to 1.9 T. A relatively large variation in the reflected base line level is observed. This is related to a shift of the resonance frequency due to the thermal expansion of the wire and the subsequent tuning of the resonator between the individual measurements (see fig. A.2 in the appendix). Remembering that the injection frequency is fixed, it leaves the extremal value of the resonance and moves on the slope, where the reflection coefficient is higher. The general behavior of the traces, however, is very similar compared to each other. According to the power

indicator of the amplifier, a threshold for the multipacting onset was found at about 10 W. This shows a reasonable discrepancy to the threshold value, predicted by the ESA Multipactor Calculator in 3.6.1 (around 18 W).

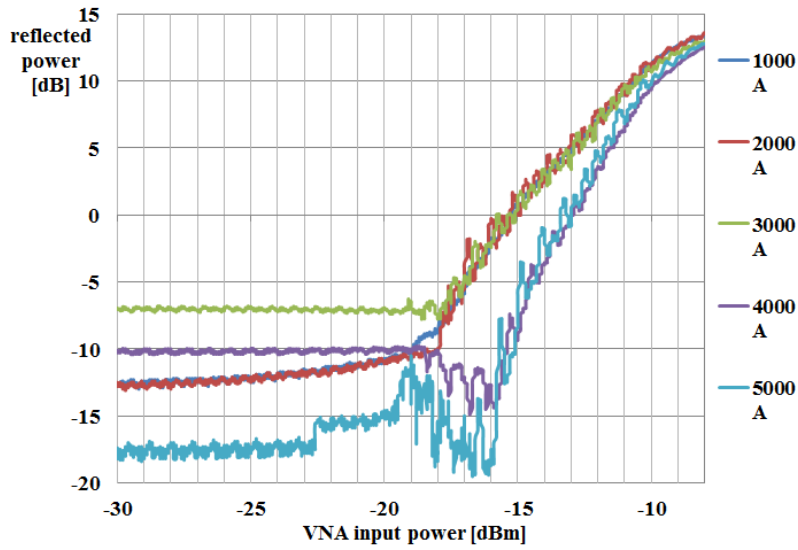


Figure 3.21: Reflected power at high magnetic fields for the uncoated beam pipe. The large variation in the reflected base level is due to thermal resonance shift.

3.7.2 Coated Chamber

After the characterization of the uncoated chamber, the dipole was opened to install a chamber coated by DCCMS sputtering. The coating covered the full inner surface. Once the wire was re-installed and the system reached proper vacuum conditions, the measurements have been repeated. The fully coated chamber shows a significantly different behavior in reflected power and outgassing. Figure 3.22 shows the reflected power over the complete magnetic field range. These measurements were performed at an injection frequency of 130 MHz. While in the uncoated chamber clear thresholds for the exponential rise in reflected power have been observed, the coated chamber generally does not exhibit any reflected power above base level besides one exception. This exception occurred during the first measurement at 3000 A. However, an immediate repetition at 3000 A didn't show any reflected power. The appearance of the exception is not understood yet. The falling signals towards the end of the power sweep are due to the compression of the amplifier. This could not be observed in the uncoated chamber because the large amount of reflected power masked the amplifier's compression.

Taking a look on the recorded pressure data, a very good correlation between pressure rise and the amount of reflected power has been found. Figure 3.23 shows the pressure recordings for the uncoated and then for the coated chamber. The pressure in the uncoated chamber (black dots) is relatively high compared to the uncoated chamber (white dots). For this case, a pronounced pressure rise can be seen in the region close to cyclotron resonance, which perfectly matches to the obtained reflected power. For the coated chamber, no pressure activity was observed up to the exceptional spike at 3000 A, resulting in a continued pressure activity (white triangles). To this pressure activity, no corresponding reflected power was detected by the VNA.

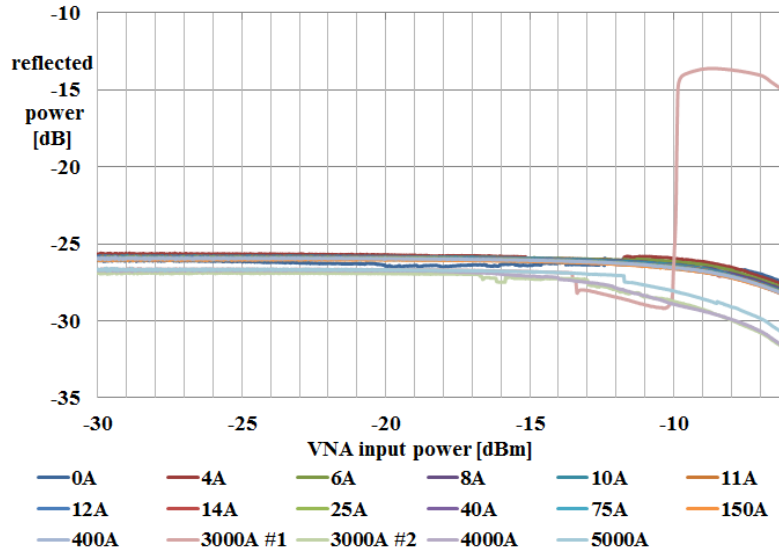


Figure 3.22: Reflected power for low and high magnetic fields on the DCCMS coated chamber. The injection frequency was 130 MHz. A clear abnormality for the first measurement at 3000 Ampere was observed.

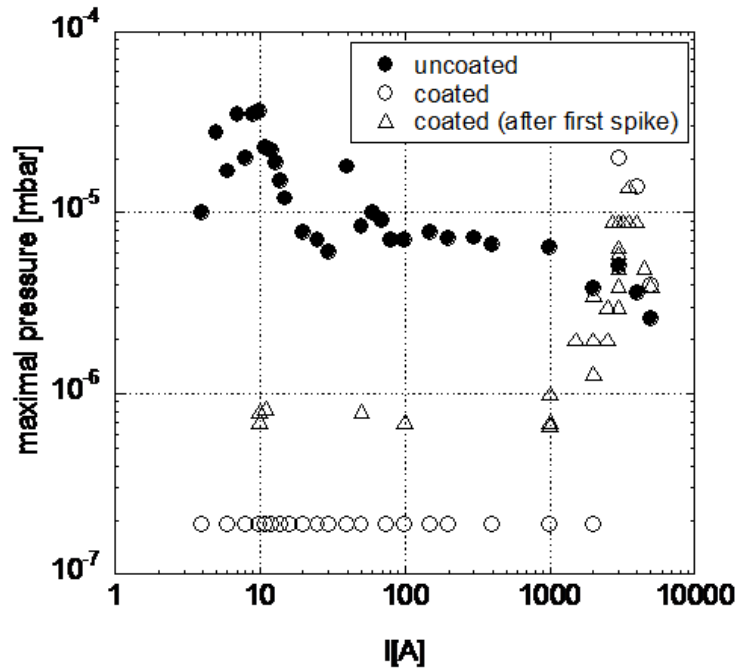


Figure 3.23: Pressure data for the uncoated and the coated chamber. A clear pronun- ciation at cyclotron resonance for the uncoated chamber (black dots) was measured. The measurements did not exhibit any pressure rise for the coated chamber (white dots). A remanent pressure activity after the exceptional multipacting event (white triangles) was observed.

The fact that the network analyzer was not able to detect this could probably be due to insufficient sensitivity as the electron cloud density was too low compared to the exceptional measurement.

3.8 Results of the DC Hollow Cathode sputtered Coating

A second type of coating, produced by DC hollow cathode sputtering (DCHCS), was tested on a different chamber. While the previous coating was produced by magnetron sputtering and covered the complete inner surface of the chamber, the hollow cathode deposition results in two carbon stripes (top and bottom) along the larger sides of the beam pipe, where most of the electrons are expected to impinge due to the confinement by the magnetic field. This coating technique does not require to open the magnet's yoke. Instead, graphite targets can be inserted directly into the beam chamber and for the sputtering process, the magnetic field of the dipole can be used. The following section starts with the characterization of the stainless steel chamber. Later on, the measurement results of the coated chamber are presented and discussed.

3.8.1 Characterization of the Stainless Steel Chamber

First, the results of the characterization of the stainless steel chamber are shown. The measurements took place after the chamber was received from chemical cleaning. Note that before these measurement runs, an additional 30 dB attenuator was inserted in the coupling branch to protect the VNA against power overloads. This results in generally lower maximum values of reflected power compared to the results of the DC magnetron sputtered coating, where no additional attenuator was implemented. This measurement run was performed at 130.12 MHz as a function of magnetic field and with a 5 seconds power sweep, resulting in a maximum output power of about 30 W. Because this was the first measurement using this chamber, 5 measurements have been done without external magnetic field. After that, two measurements per dipole current have been done. Figure 3.24 shows the results for the first measurement of each applied magnetic field (in the chronological order from blue to red).

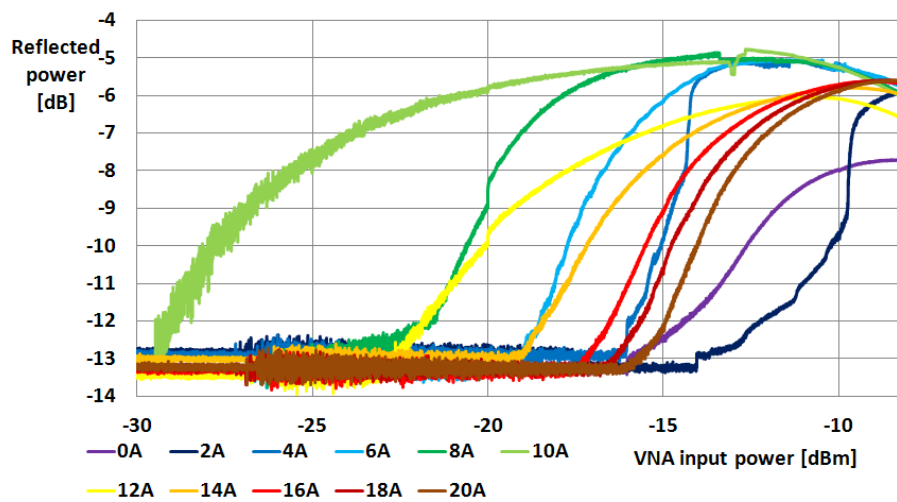


Figure 3.24: Characterization of the bare stainless steel chamber in the low magnetic field range. Measurement parameters: 130.12 MHz, 5 s power sweep ($P_{\max}=30$ W), various magnetic fields. A pronounced multipacting at cyclotron resonance was observed. The chronological order is from blue to red.

Figure 3.25 shows the comparison for the first five measurements that were performed without external DC magnetic field. It can be seen that within these measurements over a total duration of roughly 10 minutes with two minutes pause after each measurement, the surface of the chamber got some conditioning, resulting in a lower SEY. Consequently, less secondary electrons due to less sticky molecules can be desorbed and released into the vacuum. The reflected power also correlates very well with the pressure recordings which are shown in figure 3.26.

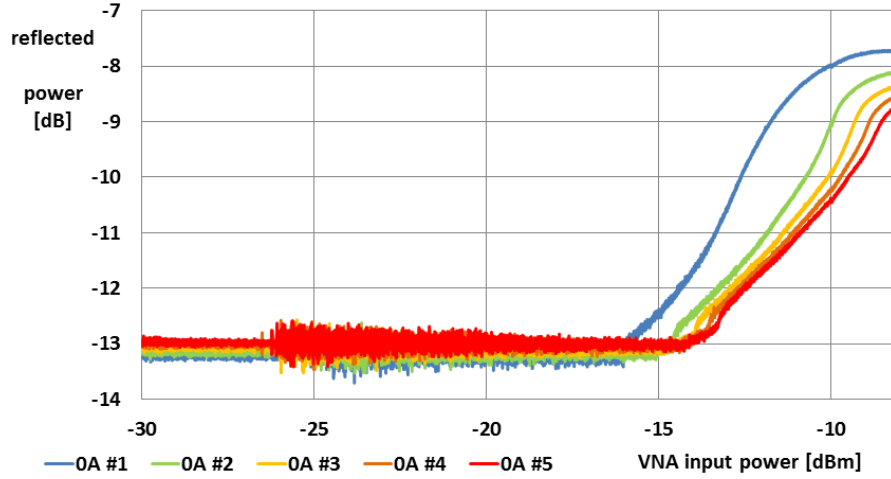


Figure 3.25: Comparison of the first five measurements without DC magnetic field. Surface conditioning (scrubbing effect) can be observed at decreasing reflected power. The chronological order is from blue to red.

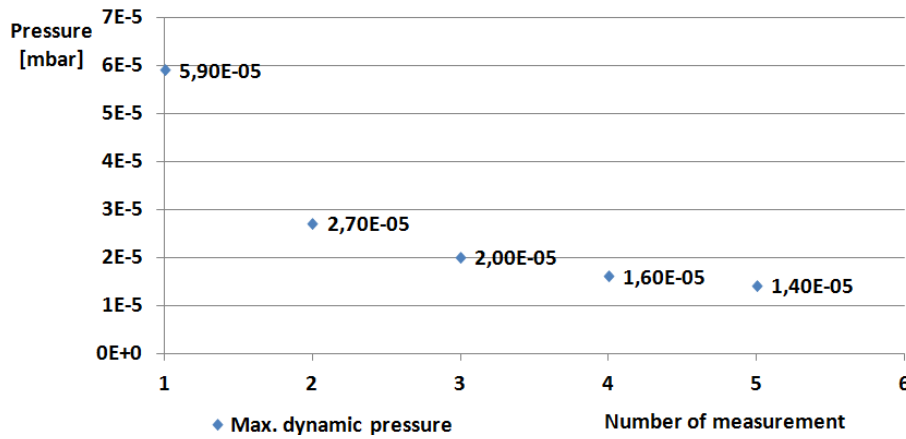


Figure 3.26: Decrease in maximum pressure is related to the conditioning of the surface and correlates very well to the obtained reflected power.

The fact that multipacting occurred so strongly without external magnetic field was unexpected for this was not observed in previous measurements, using different chambers. This led to the assumption that a remanent magnetization of the chamber could be responsible for the multipacting without applied external magnetic field. To verify this assumption the polarity of the external magnetic field has been inverted and the measurements were repeated. It was found that in order to reach the cyclotron resonance condition, a larger current had to be fed through the magnet, shifting from 10 A to 14 A. This suggests that first, a remanent field had to

be compensated before the applied current could contribute to the field inversion. Figure 3.27 shows the reflected power of the repeated measurement with an inverted magnetic field. It can be clearly seen that the cyclotron resonance condition shifted to a larger current.

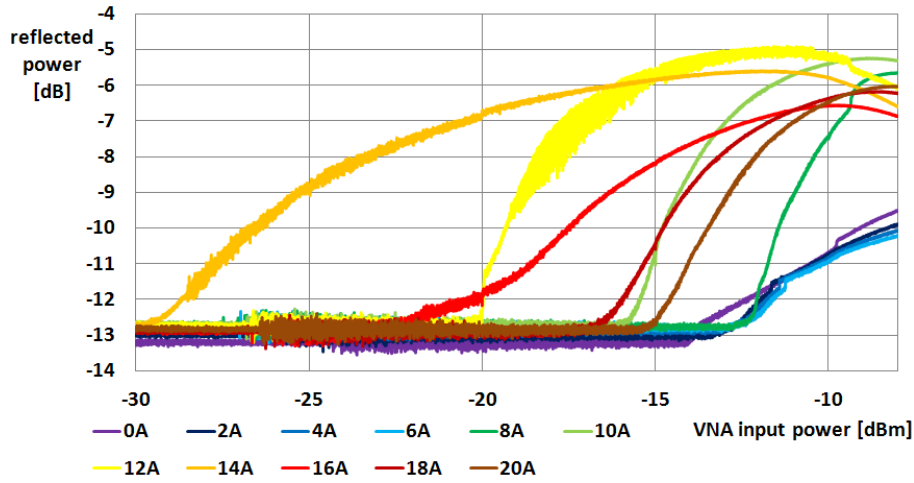


Figure 3.27: Characterization of the chamber with inverted magnetic field. Cyclotron Resonance shifted to a necessary current of 14 A in order to get reached. The chronological order is from blue to red.

These results gave reason to measure the apparently remanent magnetization of the chamber with a Hall-probe. The probe was connected to a long stick so that the magnetic field could be measured over a reasonable distance into the chamber, beginning at the front aperture of the pumping port. This also yielded valuable information about the characteristic of the fringe field. Figure 3.28 shows the magnetic field values vs a partly length at the beginning of the dipole without external magnetic field. The measured background was -0.3 Gauss.

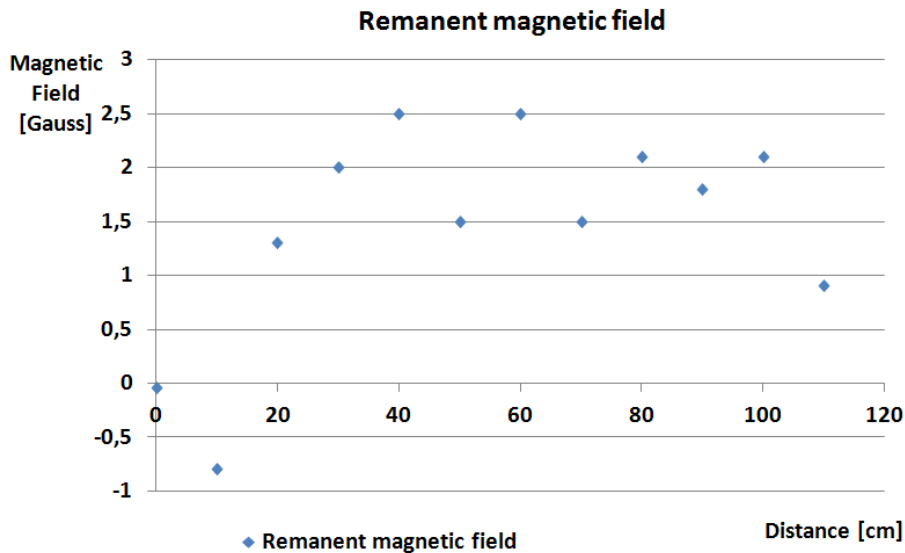


Figure 3.28: Remanent magnetic field (no externally applied field) for the first 110 cm of the dipole including trend line.

In addition, measuring the magnetic field with a Hall-probe made it possible to verify the correlation between applied current through the magnet and its resulting

magnetic field as it was shown in the transfer function of a reference dipole. Because of the transfer function's non-linearities at both extremities, no true current values could be extracted but they were easier to estimate. In order to verify the transfer function, a current of 11 A was applied to the magnet, since this was the estimated current providing a magnetic field of 4.6 mT, which meets the cyclotron resonance for 130 MHz. Figure 3.29 shows the measured magnetic field whilst applying a current of 11 A:

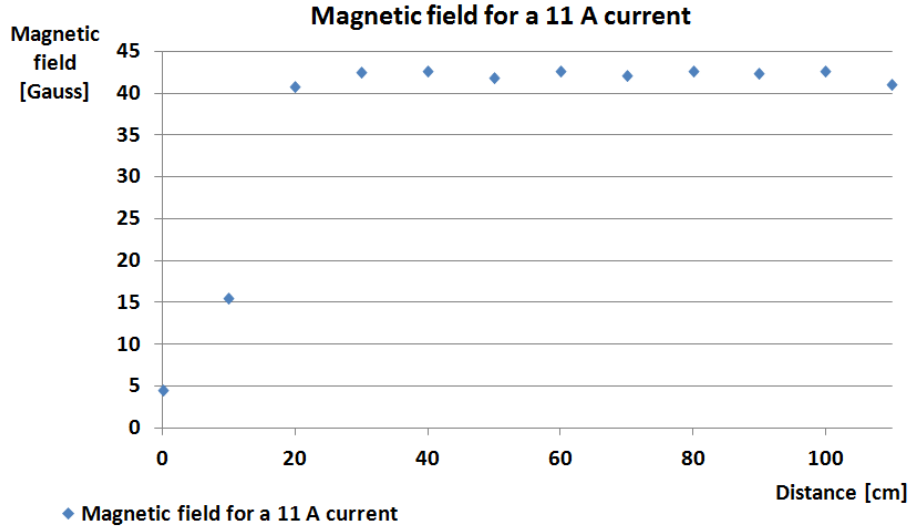


Figure 3.29: Magnetic field with a current of 11 A applied to the magnet.

This confirms the 11 A, which have been estimated to be necessary for a magnetic field of 4.6 mT. It also shows, that the transfer function can be used to make reliable relations between current and generated magnetic field. Knowing the direction and amplitude of the remanent field, it is possible to induce multipacting exactly on cyclotron resonance without searching for it before.

3.8.2 Coated Chamber

After the application of the DC hollow cathode coating, tests have been repeated on a frequency of 130.25 MHz with a power sweep from -30 dBm to -8 dBm over 5 seconds by the network analyzer and as a function of magnetic field. The first measurement without external magnetic field showed a small increase in reflected power towards the end of the power sweep and a reasonable pressure rise was observed. For consecutive measurements, the reflected power and pressure rise was low and very stable over all applied magnetic fields but did not completely disappear like in the chamber which was fully coated by magnetron sputtering. Fig. 3.30 shows the first measurements with this coated chamber in the low magnetic field range (in the chronological order from blue to red colors). It is very noticeable that the reflected power, as well as the pressure, are apparently independent from the magnetic field strength. Even around cyclotron resonance condition, no change in the diagnostics nor a formation of plasma in the chamber could be observed. The same behavior applied for tests with high magnetic fields. This could be an indication, that the multipacting did not take place in the dipole section but somewhere else in the test stand, where the magnetic field does not affect the free electrons. This remanent multipacting is in the following referred to as parasitic multipacting.

A pressure comparison of the uncoated and the coated chamber also shows a very good reduction in electron-stimulated desorption. Fig. 3.31 shows the pressure versus dipole current for the uncoated and the coated chamber. For the uncoated chamber, the pressure rise has a pronounciation at cyclotron resonance (10A), which was observed in former measurements using uncoated chambers. The DCHCS coated chamber does not exhibit a significant pressure rise. The fact that the maximum pressure without external field is almost the same is an indication for an unclean surface due to air exposure during re-assembling the system.

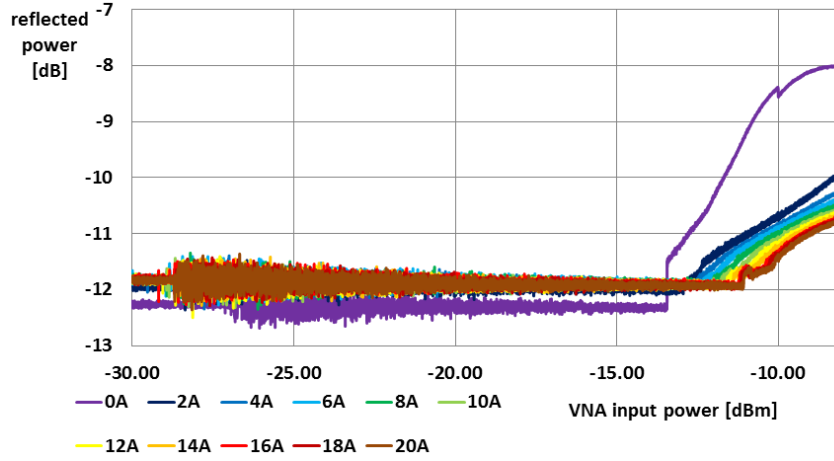


Figure 3.30: Reflected power of the DCHCS coated chamber in the low magnetic field range. Initial scrubbing can be detected for the first measurement without external field. Small amounts of multipacting, quasi-independent from the magnetic field. The chronological order is from blue to red.

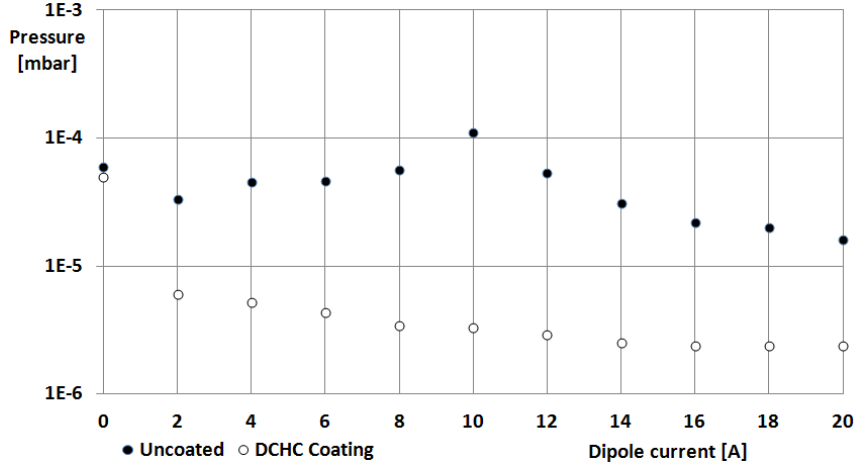


Figure 3.31: Pressure comparison of the uncoated and DCHCS coated chamber in the low magnetic field range. The uncoated chamber shows a pronounced pressure rise at cyclotron resonance (10A), while the coated chamber does not exhibit any significant pressure rise.

These tests have been repeated using a continuous wave frequency of 83.86 MHz, which is another resonant frequency of the set-up. On this frequency, however, no reflected power was observed. Figure 3.32 shows the reflected power in the low magnetic field range in the chronological order from blue to red lines.

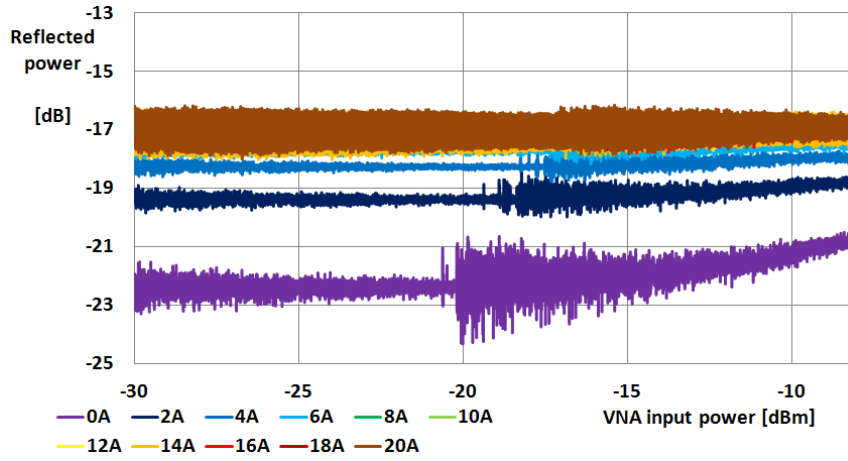


Figure 3.32: Reflected power of the DCHCS coated chamber at 83.86 MHz. Due to the better mode coupling, the base line reflected power is significantly lower and thus, sensitivity to small amounts of multipacting increases. The chronological order is from blue to red.

At this frequency it is very noticeable that the base line level for the first measurement without external magnetic field is much lower (around -22 dB) compared to the measurements at 130 MHz in fig. 3.30 (around -12 dB). The difference can be explained by the much better mode coupling for 83.86 MHz, reducing significantly the amount of base line reflected power. This generally increases the sensitivity to very small amounts of multipacting, which otherwise would be superimposed by the background. Figure 3.33 shows the resonances during these measurements. It can be seen that the coupling for 83 MHz is clearly better than for 130 MHz. Yet, a better matched resonance with a steep gradient is much more susceptible to thermal drift, resulting in a strong worsening of the base line level with ongoing measurements. It continues until a thermal equilibrium of the wire is reached, depending on input power and waiting time between the individual measurements. This effect can even be seen during the first few measurements in fig: 3.32, where the reflected power increases during the measurement due to thermal drift. Thus, it is evident that thermal drift, especially when a high sensitivity is necessary, is a major limitation to this set-up.

Additional measurements of this kind have been performed using all resonances shown in fig. 3.4. Here, just the resonances at 130 MHz and 101 MHz show the parasitic multipacting, which is independent from the magnetic field. At all other resonances, no parasitic multipacting could be observed. This supports the hypothesis that the parasitic multipacting happens outside the coated dipole section, dependent on the standing wave pattern of the particular resonances.

The hypothesis could be proved by setting up a model of the dipole in CST Microwave Studio, including the pre-chamber and the exact geometry of the pumping port and the connected bellows between the pre-chamber and the dipole, as well as between the far end of the dipole and the closing flange. These regions are uncoated and could be exposed to multipacting at certain frequencies. Since the measurement results showed clearly on which frequencies the parasitic multipacting occurred, they can be compared to the simulated standing wave pattern of the complete model in

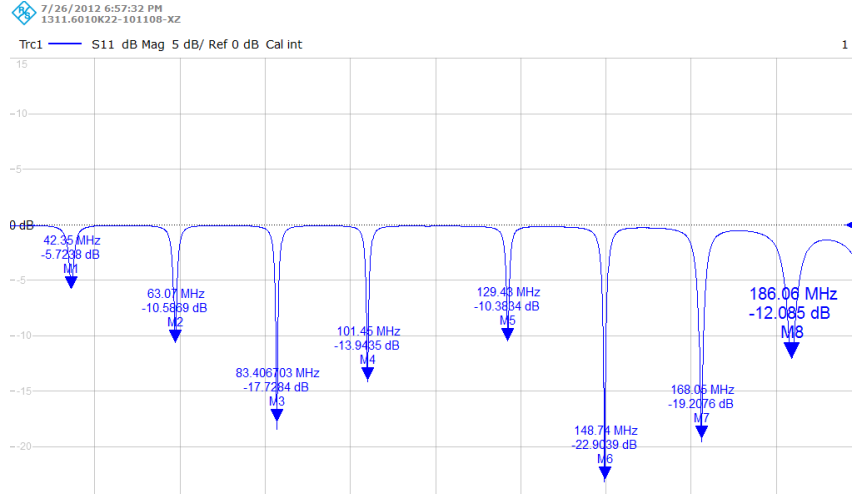


Figure 3.33: Reflected power of the DCHCS coated chamber at 83.86 MHz. Due to the better mode coupling, the base line reflected power is significantly lower and thus, sensitivity to small amounts of multipacting increases.

order to localize the parasitic multipacting. Measurements with high magnetic fields did not yield different results and hence, are not mentioned further.

3.9 Spin-off Applications of the Test Stand

As a possible spin-off application, the technique of the multipacting test stand could possibly be applied to LHC injection kicker magnets (MKI-type), where it is used to scrub the copper bypass tube via induced multipacting. Here, it is taken advantage of the formerly observed conditioning effect by electron bombardment on the SPS stainless steel chambers. According to simulations using the ESA Multipactor Calculator, the multipacting onset takes place at very low RF power of around 4.5 Watt. Since the multipacting is located at the electric field maxima with respect to the standing wave pattern, higher order modes can be used for power injection, additionally to the fundamental mode. Also, the wire can be terminated with a short circuit and an open circuit, changing the standing wave pattern. In combination, these two measures could provide a uniform cleaning of the bypass tube. In order to connect the 100 CONFLAT flange of the kicker tank to the standard SPS flanges, adapter flanges will be necessary.

At both ends of the bypass tube, there are RF fingers. These structures provide a proper electrical interconnection of different tube sections. Since the RF output power would be around 35 W, it is crucial to know how much of the power is dissipated in the tungsten wire and in the copper tube to prevent damage to the RF fingers. Good estimations can be achieved by calculating the power losses for the wire and the copper tube, respectively. The used formulas and background theory are extracted from [23].

The specific power loss of the two conductors in a coaxial transmission line is given by equation 3.4

$$p_v \approx 2 \cdot \alpha_R \cdot P \quad (3.4)$$

where p_v is the specific power loss in the conductors, α_R the resistance loss and P the input power. Since the inner and the outer conductor consist of two different materials, the resistance loss has to be calculated separately for each conductor and the specific power loss for this case can be described as shown in equ. 3.5

$$p_v \approx 2 \cdot (\alpha_W + \alpha_{Cu}) \cdot P \quad (3.5)$$

where α_W is the resistance loss of the tungsten wire and α_{Cu} the resistance loss of the copper tube. They can be derived by the resistance load per unit length and the RF sheet resistance of the conductors. The RF sheet resistance considers the current displacement towards the conductors' surfaces, operating at high frequencies. This is referred to as the Skin-Effect, meaning that the effective conducting cross-section is given by the product of the conductors' circumference and the skin-depth δ .

The skin-depth can be calculated using equ. 3.6

$$\delta = \frac{1}{\sqrt{\pi \cdot f \cdot \mu_0 \cdot \mu_r \cdot \sigma}} \quad (3.6)$$

where f is the RF frequency, μ_0 and μ_r the vacuum permeability and the relative permeability and σ the electrical conductivity. The fundamental mode of the set-up was measured as 35.7 MHz. The electrical conductivity of different materials can easily be found in the web or in literature and gives $\sigma_W = 18.52 \cdot 10^6 S/m$ for tungsten and $\sigma_{Cu} = 58 \cdot 10^6 S/m$ for copper. The vacuum permeability is $\mu_0 = 4 \cdot \pi \cdot 10^{-6} H/m$ and the relative permeability is one for both materials. Since all parameters are known, the skin-depth of tungsten and copper can be calculated to 19.6 μm and 11.6 μm , respectively. Afterwards, the RF sheet resistance can be obtained by the inverse product of skin-depth and conductivity, shown in equ. 3.7:

$$R_s = \frac{\rho}{\delta} = \frac{1}{\sigma \cdot \delta} \quad (3.7)$$

where R_s is the RF sheet resistance, ρ the electrical resistivity, σ the electrical conductivity and δ the skin-depth. Applying equ. 3.7 to the parameters of the two materials, it yields a RF sheet resistance of $2.75 \cdot 10^{-3} \Omega$ for tungsten and $1.48 \cdot 10^{-3} \Omega$ for copper. Since the skin-depth is considered in the RF sheet resistance, one can calculate the resistance load per unit length in the same way as if it would be done in the case of direct currents. Thus, the RF sheet resistance can be divided by the circumference of the conductors, using the real dimensions instead of calculating their effective cross-sectional areas. The resistance load per unit length is given by equ. 3.8

$$R' = \frac{R_s}{\pi \cdot d} \quad (3.8)$$

where R' is the resistance load per unit length and d the diameter of the conductor, which is $0.5 \cdot 10^{-3} m$ for the tungsten wire and $53.7 \cdot 10^{-3} m$ for the copper bypass tube. Inserting the respective parameters in equ. 3.8, the resistance load for the wire

calculates to $1.75 \frac{\Omega}{m}$ and for the copper tube to $8.77 \cdot 10^{-3} \frac{\Omega}{m}$. The resistance loss α_R can be calculated using equ. 3.9

$$\alpha_R = \left(\frac{R'_W}{2 \cdot Z_L} + \frac{R'_{Cu}}{2 \cdot Z_L} \right) \cdot 8.686 \quad (3.9)$$

where R'_W and R'_{Cu} are the resistance loads per unit length for tungsten and copper and Z_L the characteristic impedance of the coaxial transmission line. The characteristic impedance was measured via time domain reflectometry and is 280.6Ω (see 3.5.2). The factor 8.686 is due to the conversion of nepers/m to dB/m. The total resistance loss then is calculated to

$$\alpha_R = \left(\underbrace{\frac{1.75 \Omega}{561.2 \Omega}}_{3.11 \cdot 10^{-3} \text{ nepers/m}} + \underbrace{\frac{8.77 \cdot 10^{-3} \Omega}{561.2 \Omega}}_{15.62 \cdot 10^{-6} \text{ nepers/m}} \right) \cdot 8.686 = 27.22 \cdot 10^{-3} \text{ dB/m} \quad (3.10)$$

Considering the losses for each material separately, it yields $\alpha_W = 27.1 \cdot 10^{-3} \text{ dB/m}$ for the tungsten wire and $\alpha_{Cu} = 135.7 \cdot 10^{-6} \text{ dB/m}$ for the copper tube. Recalling the total loss of $27.22 \cdot 10^{-3} \text{ dB/m}$, it becomes clear that 99.5% of the material losses account to the tungsten wire. Thus, no damage due to a thermal overload of the RF fingers is expected, when applying this technique to the MKI-type kicker magnet. In order to calculate the absolute dissipated power, equ. 3.5 can be used. Considering an output power of 35 Watt, the total resistance loss calculates to

$$p_v \approx 2 \cdot (\alpha_W + \alpha_{Cu}) \cdot P \approx 2 \cdot 27.22 \cdot 10^{-3} \text{ dB/m} \cdot 35 \text{ W} \approx 1.91 \text{ W/m} \quad (3.11)$$

Since the length of the copper bypass tube is 3140 mm, the total dissipated power, distributed over the complete copper tube and the tungsten wire would be around 6 Watt, while the major part will be dissipated in the tungsten wire. Hence, applying this technique should not do damage to the RF fingers.

When removing the electronics, i.e. the residual gas analyzer and the pressure gauges, it is possible to bake out the system in order to make it compatible with the ultra-high vacuum (a few 10^{-11} mbar) of the LHC injection kicker magnets. Because the effect of the bakeout after scrubbing the magnet is not known, it is proposed to scrub after bakeout. When valves are installed after bakeout, the wire would be put through the appropriate bypass tube. Some kind of release mechanism has to be designed in order to withdraw the wire easily after scrubbing. A set-up, consisting of a copper tube, RF fingers and a vacuum tank could be used to verify the procedure before applying it to the kicker magnets.

4. E-Cloud Diagnostics by Means of Microwave Transmission

4.1 Goal of the diagnostic Method

In 2010, a set-up for performing in-situ microwave diagnostics of the electron cloud in the SPS has been installed at access point BA5. The goal of this set-up is to verify beneficial effects of electron cloud mitigation techniques (e.g. carbon coatings, clearing electrodes) under real beam conditions, additionally to existing diagnostic methods like the observation of pressure rise and e-cloud monitors.

4.2 Principle

The principle of this method is the analysis of the phase modulation (PM) of an injected continuous wave which serves as carrier wave in the set-up. The phase shift of the carrier wave is caused by the beam induced electron cloud. It is given by equation 4.1 [24]:

$$\Delta\varphi = \frac{L\omega_p^2}{2c(\omega^2 - \omega_c^2)^{\frac{1}{2}}} = \frac{L\sqrt{\frac{n_e e^2}{\epsilon_0 m_e}}^2}{2c(\omega^2 - \omega_c^2)^{\frac{1}{2}}} \cong \frac{L \cdot 3181 n_e}{2c(\omega^2 - \omega_c^2)^{\frac{1}{2}}} \quad (4.1)$$

where ω is the injected frequency, L the transmission length, ω_c the cutoff frequency of the waveguide, c the speed of light, ω_p the plasma frequency, ϵ_0 the permittivity in free space, e the electron charge, m_e the electron mass and n_e the number of electrons per square meters. Note that this equation assumes a nearly lossless transmission. This means that there are no internal and external reflections, causing resonances. Since the beam cycles many times in the machine whilst recording, the integrated electron cloud density is measured.

In the frequency domain the modulation appears in sidebands, located at the positive and negative distance of the modulation frequency from the centered carrier frequency. In the case of the SPS, the phase modulation occurs at 43.35 kHz (23 μ s), which is the revolution frequency. Thus, the phase modulated electron cloud signal

is to be expected at this frequency. Figure 4.1 shows the spectrum as it appears on the screen of the vector spectrum analyzer during recent measurements. In the spectrogram, it can be clearly seen that the electron cloud induced signal at SPS revolution frequency shows up simultaneously with the batch injection, which is indicated by the starting point of the beam induced signals. Additionally, a reference signal at 42 kHz is applied, either amplitude-modulated (AM) or phase-modulated (PM), depending on whether it is intended to check $AM \rightarrow PM$ or $PM \rightarrow AM$ conversion. Measurements with both, a phase-modulated and an amplitude-modulated reference signal have been recorded.

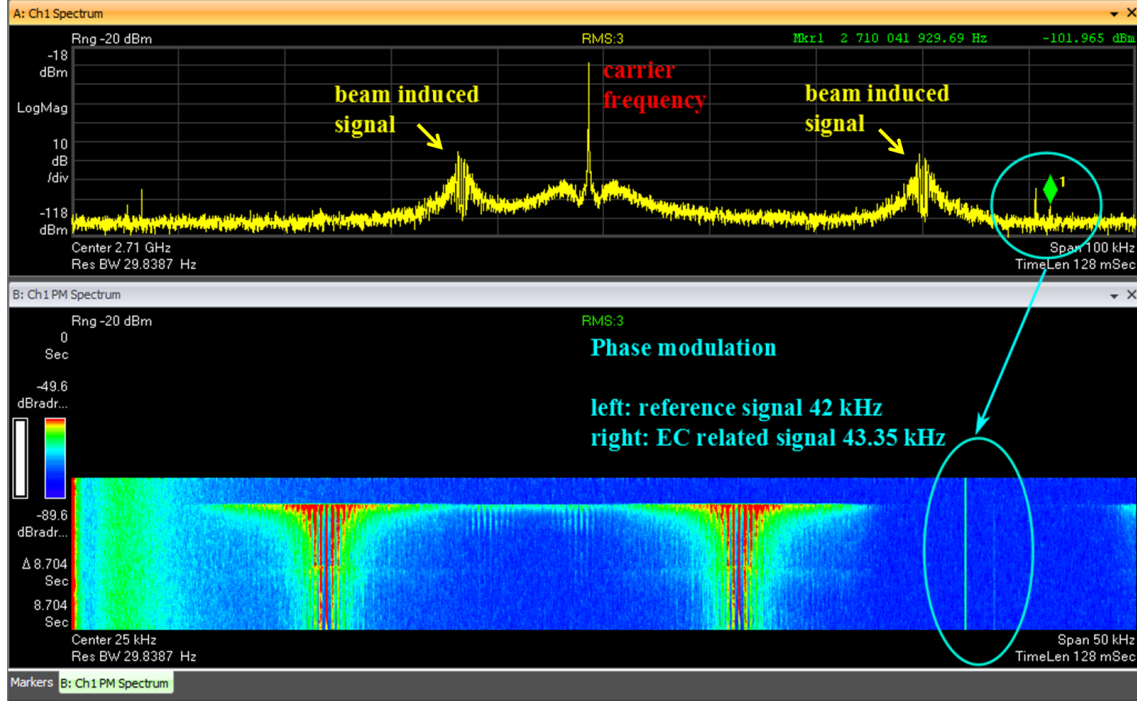


Figure 4.1: Top: Spectrum of a recent sample measurement. The electron cloud (EC) signal is marked and accompanied by a PM reference signal. Bottom: Phase-demodulated spectrum in spectrogram mode. Batch injection can be seen via the beam induced signals.

4.3 Set-Up 2011

Figure 4.2 shows the experimental set-up in the year 2011. Hereby, three coupling loops were implemented in the SPS. One antenna served as sending antenna, where a carrier wave was injected. This antenna was placed between two MBB-type dipoles, whereas one dipole was coated and the other one was uncoated. At the end of each dipole, there was a receiving antenna, catching up the carrier wave after passing the dipoles. It was expected, that after passing the 6.5 meter long dipoles, the carrier wave in the uncoated dipole encountered a phase modulation, whereas the carrier wave passing the coated dipole did not encounter any detectable phase shift [25].

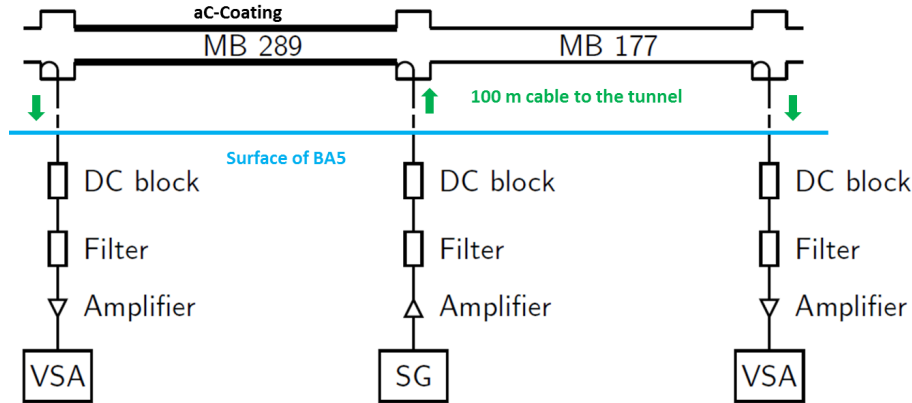


Figure 4.2: Transmission measurements in a coated and an uncoated MBB-type dipole. The carrier wave is injected through the center coupling loop and transmitted to both sides.

In a brief, these expectations were matched by the obtained results, performing measurements with various beam parameters (e.g. beam intensity, bunch spacing). Figure 4.3 shows the results for a beam with nominal intensity and a 25 ns bunch spacing. The uncoated chamber clearly exhibits a rise in phase modulation at SPS revolution frequency, which increases with additional batch injections. The coated chamber does not exhibit any detectable phase modulation of the carrier wave, which indicates the absence of electron cloud. Thus, this set-up easily provided first qualitative information on the efficiency of the carbon coating used in the dipole. Due to the fact that the electronic components were located in the tunnel, they got quickly damaged by radiation during beam operations. Therefore, it was decided to transfer these components to the surface and to install cables to provide the connection to the antennas in the accelerator.

4.4 Set-Up 2012

Recently, it was in the interest to evaluate the feasibility to measure over the length of two consecutive, uncoated dipoles and possibly also to verify the conditioning of these dipoles during a one week long scrubbing run. Therefore, the set-up has been changed as shown in figure 4.4. In this work, the set-up and the obtained results are written as in [26].

During these measurements the signal generator injected a 10 dBm carrier wave of 2.71 GHz which was at a maximum in transmission according to the hardware

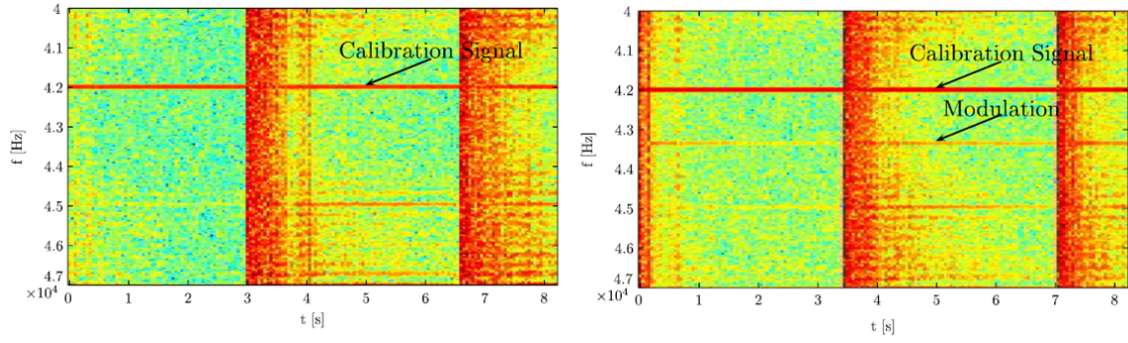


Figure 4.3: Spectrogram mode of the phase-modulated frequency part in the uncoated (left graph) and coated (right graph) section. The red peaks correspond to the injection of a new batch. This measurement was performed with the nominal LHC 25 ns beam of four batches at SPS. Magnetic field at flat bottom.

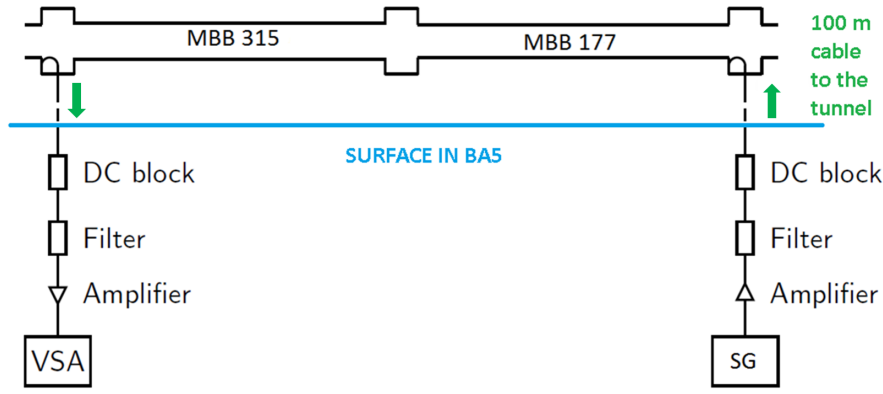


Figure 4.4: Transmission measurements over two consecutive uncoated MBB-type dipoles. SG: Signal Generator, VSA: Vector Spectrum Analyzer

transfer function. As calibration signal, either a phase modulation with 1 mrad or an amplitude modulation with 1% of the carrier amplitude was applied with a frequency of 42 kHz. Afterwards, the data of both frequencies, the calibration signal and the phase-modulated electron cloud signal, were filtered by software from the recordings and could be displayed over time. As resolution bandwidth of the spectrum analyzer, 100 kHz was set.

4.4.1 Results

The first measurements were taken with a vector spectrum analyzer which had a rather small size of internal memory. This limited the recording time to 8 seconds. Thus, it has been triggered manually just before the injection of the last batches. The base level in the phase-modulated signal can be obtained from the signal level for the empty machine. Figure 4.5 shows a measurement for the empty machine after a beam dump. It can be seen that the PM base line level is at -71 dB compared to 1 rad. For all subsequent measurements, this is considered as reference level. The calibration signal shows an average level of -60 dB which matches the 1 mrad set on the signal generator.

Figure 4.6 shows the results for a beam with 4 batches, 25 ns spacing and a maximum total intensity of $3455 \cdot 10^{10}$ protons. The number of protons was extracted from

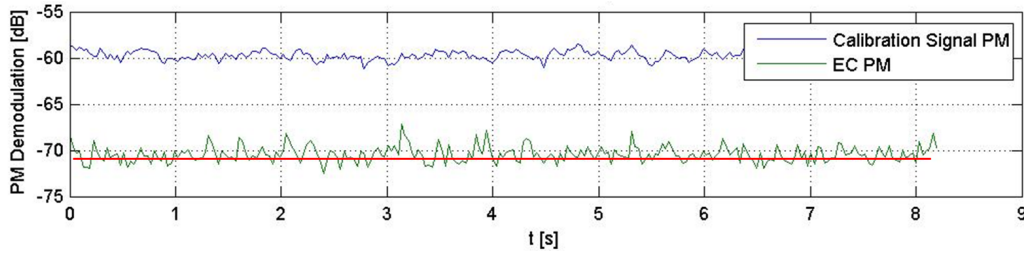


Figure 4.5: Time trace of the electron cloud induced signal (EC) and the calibration signal for an empty machine. Obtained average base level is around -71 dB (red line).

the data measured by the beam current to current transformer (BCCT). In this measurement, a small increase in phase modulation can be seen. The displayed traces were recorded just after the injection of the fourth batch. Compared to the base line level obtained above, one can see that the e-cloud signal has risen 4 dB up to -67 dB. This signal was completely reproducible for the following beams with similar beam parameters.

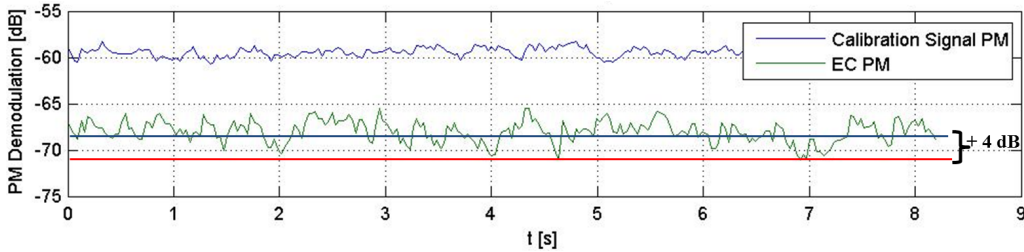


Figure 4.6: Time trace of an increased electron cloud induced signal compared to base level around -67 dB. 4 batches, 25 ns spacing and a maximum total intensity of $3455 \cdot 10^{10}$ protons.

During the scrubbing run, the vector spectrum analyzer was replaced by a new one with a larger amount of internal memory. Thus, it was possible to record complete supercycles and the manual trigger was not necessary anymore. According to the data sheets, the two spectrum analyzers are equal in terms of sensitivity and accuracy. Therefore, all taken measurements are directly comparable. Subsequently, the dynamic behavior of the e-cloud signal could be observed. For the measurement shown in fig. 4.7, the beam parameters were one batch, 25 ns spacing and a maximum total intensity of $1274 \cdot 10^{10}$ protons. Taking a look at the time traces, one can see a very slight increase in electron cloud phase modulation which is an indication that an electron cloud is present (red box). This occurs at 18 seconds, where the batch injection took place. Batch injections can be identified by spikes in the amplitude-modulated part. The previous signals in this time trace are due to injection and acceleration of a low-intensity beam.

In the measurement which corresponds to fig. 4.8 (red box) the results with two batches, 25 ns spacing and a maximum total intensity of $2530 \cdot 10^{10}$ protons are shown. At 32 seconds, where the second batch injection took place, a clear step in PM can be observed. Since the integrated electron cloud density is measured, the rise is related to the longer and also more dense presence of electron cloud due to two consecutive batches, accumulated over many beam revolutions in the ring. The magnitude of phase modulation after injection of the second batch can be extracted

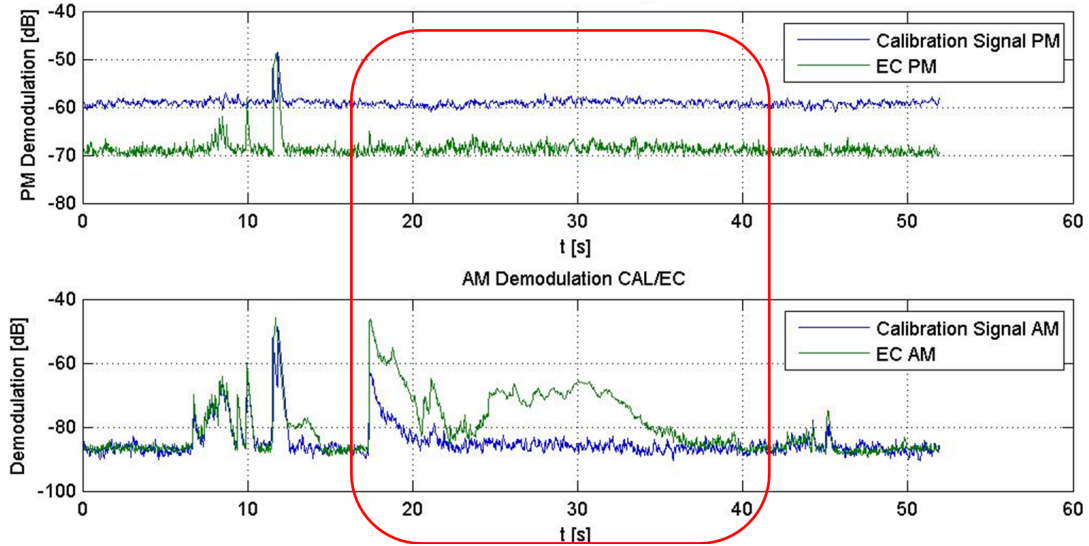


Figure 4.7: High intensity beam (red box): One batch, 25 ns spacing and a maximum total intensity of $1274 \cdot 10^{10}$ protons. Small increase in e-cloud PM signal since batch injection at 18 seconds (top). Batch injection can be identified by spikes in AM (bottom).

from the time trace and gives roughly -62 dB , which is $+9 \text{ dB}$ with respect to the reference level at -71 dB .

The previous signals (blue box) are due to an injection and an acceleration of a low intensity beam with one batch, 25 ns spacing and a maximum total intensity of $871 \cdot 10^{10}$ protons. One can see that the spectrum analyzer is dazzled by the changing RF due to beam acceleration. During the presence of this beam, no e-cloud could be observed. Note that for this measurement an AM reference signal was applied and thus it appears in the AM part. Also, a weak signal at the reference signal frequency (42 kHz) in PM, which is cannot be seen well in the time traces for it is almost indistinguishable from the background, has been observed. This means that there is a slight AM to PM conversion, which is probably due to some slope in the hardware transfer function (HTF) of the measurement set-up. Unevenness in the HTF may cause different transmission coefficients for the lower side band and the upper side band, resulting in a mixture of AM and PM. Here, it has been measured upstream (against beam direction).

The parameters for the high-intensity beam in fig. 4.9 (red box) are 3 batches, 25 ns spacing and a maximum total intensity of $3639 \cdot 10^{10}$ protons. The results for this measurement are as expected. An additional step in the e-cloud signal after injection of the third batch is clearly visible. For the low intensity beam (blue box) with the same parameters like in the previous measurement, no electron cloud could be detected neither. This measurement was performed downstream (in beam direction).

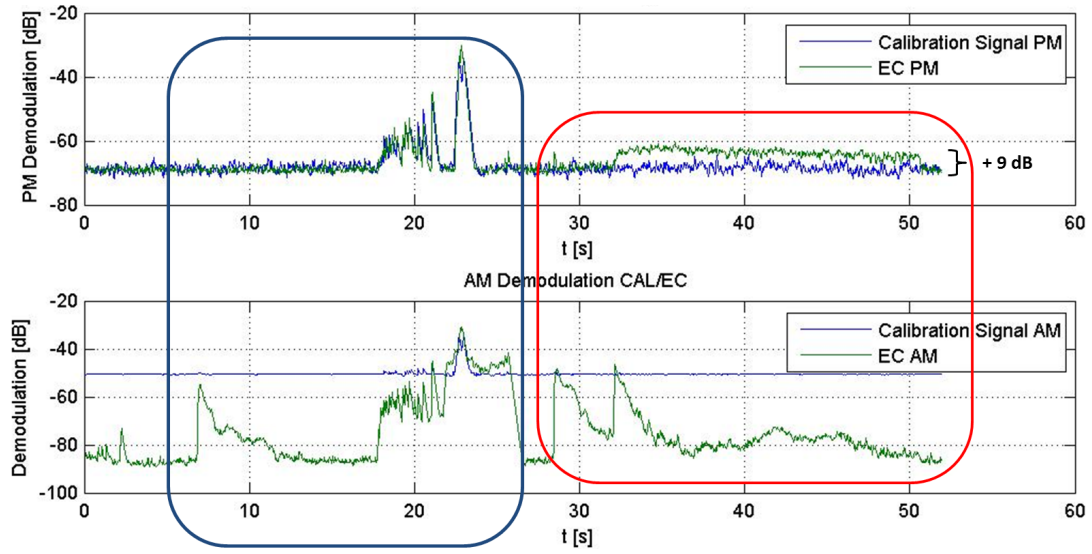


Figure 4.8: Clear step in PM e-cloud signal after the second batch of the high intensity beam at 32 s (top). Injections visible in AM part (bottom). High intensity beam (red box): Two batches, 25 ns spacing and a maximum total intensity of $2530 \cdot 10^{10}$ protons. Low intensity beam (blue box): One batch, 25 ns spacing and a maximum total intensity of $871 \cdot 10^{10}$ protons (no e-cloud). Measurement direction was upstream.

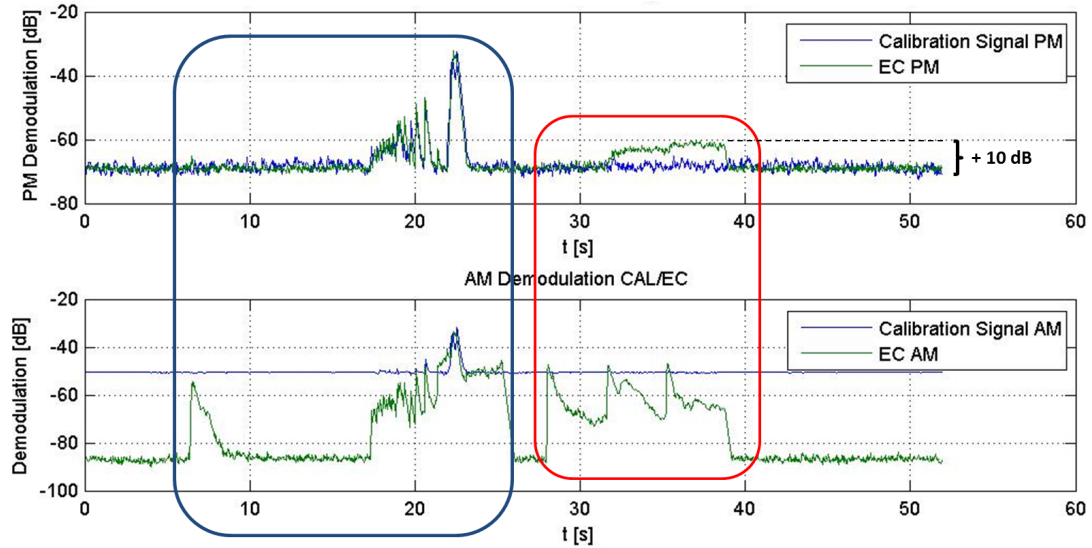


Figure 4.9: Clear step in e-cloud signal for the high intensity beam after second and third batch at 32 s and 35 s, respectively. High intensity beam: 3 batches, 25 ns spacing and a maximum total intensity of $3639 \cdot 10^{10}$ protons. Low intensity beam: One batch, 25 ns spacing and a maximum total intensity of $872 \cdot 10^{10}$ protons (no e-cloud). Measurement direction was downstream.

5. Conclusions and Outlook

5.1 Multipacting Test Stand

In the frame of the LHC luminosity upgrade, electron cloud in the SPS is considered as major limitation to the beam quality. This work focused on experimental studies, investigating the suppression of the multipacting effect by amorphous carbon coatings. Therefore, a multipacting test stand, using a resonant coaxial waveguide configuration, was set up in order to induce multipacting intentionally by RF power. The inner conductor of the coaxial set-up consists of a tungsten wire, while the outer conductor is a SPS beam chamber. The principle of operation and the commissioning of the set-up were described in detail (see chapter 3). Additionally, simulations have been made in order to estimate the power threshold of the multipacting onset for the given waveguide configuration.

At the characterization of the first stainless steel chamber, it was found that the multipacting effect is clearly enhanced when the power injection frequency and the external magnetic field fulfill the conditions for cyclotron resonance. Pronounced signals in both, reflected power and particle-stimulated desorption were obtained. Under these conditions, a glow discharge in the blue visible spectrum was observed. Afterwards, a carbon coating was applied to the chamber by DC cylindrical magnetron sputtering. The multipacting tests on the coated chamber did not yield reflected power and pressure rises due to particle-stimulated desorption. In a single measurement, reflected power was observed, followed by small dynamic pressure rises for all consecutive measurements. Overall, this coating showed a complete suppression of the multipacting effect and the subsequent electron cloud build-up, for the available input power.

A second chamber was characterized and the previously obtained results could be verified. In addition, ambiguous results concerning cyclotron resonance were obtained when switching the polarity of the external magnetic field. When investigating this issue, a remanent magnetization of the chamber was found. On this chamber, a different carbon coating was applied by DC hollow cathode sputtering. Multipacting tests showed small amounts of reflected power and pressure rise. These signals are independent from the external magnetic field, which leads to the assumption that

the measured multipacting is outside the magnet. In addition, the multipacting only occurred at certain injection frequencies which result in different standing wave patterns. This supports the hypothesis of multipacting outside the dipole. Besides the small amount of multipacting, the DCHCS coating showed a very good suppression of electron cloud and would probably be sufficient to mitigate the electron cloud in the SPS. If this can be verified, the total costs of a large scale coating process would significantly reduce for the magnets would not need to be dismantled.

It was found that the thermal expansion of the wire and the resulting mismatching is the most limiting part of the test stand in terms of sensitivity. A possible cure to this issue could be the implementation of a spring system, keeping the wire constantly straight and compensating the thermal expansion. Alternatively, the wire could be replaced by a thin and solid rod of copper beryllium. This alloy is characterized by a very high mechanical strength, which would allow to insert the rod over the complete length of the system without installing additional supportive structures inside the chamber. Its ability to preserve its shape could prevent shifting resonances due to thermal expansion. Being a copper-based alloy, it has a much higher electrical conductivity compared to tungsten, resulting in a higher Q and in the reduction of material losses as well as storing more energy in the electromagnetic field instead. When the extraction of quantitative information is of interest, the frequency-dependency of the coupling factor of the directional coupler is disruptive. Therefore, new directional couplers have been ordered, which assure a constant coupling factor over the complete operating frequency range of the set-up.

5.2 Microwave Transmission Measurements

A diagnostic tool to measure the integrated electron cloud density by means of microwave transmission was set up in a section of the SPS in 2010. Recent measurements during the annual scrubbing run yielded clear phase modulations of the carrier wave, when operating the SPS with high intensity and 25 ns bunch spacing LHC beams. For the amplitude of the phase modulated sidebands, a clear dependency of total beam intensity and number of batch injections was found. When operating with low intensity beams, no phase modulation was measured, which indicates the absence of electron cloud. During acceleration, this set-up is not able to detect the electron cloud-induced phase modulation, because it is superimposed by RF-induced signals. Thus, the set-up is limited to measure at flat bottom (magnetic field at beam injection) or flat top (magnetic field strength after acceleration at beam extraction).

This method has proven to be a very valuable diagnostic tool to detect electron cloud during scrubbing and machine development runs. The replacement of the old spectrum analyzer by a more recent model with larger internal memory already made it possible to record complete supercycles in the machine, which already improved this method much. For future measurements, the resolution bandwidth could be increased from 100 kHz to 1 MHz in order to include several harmonics of the phase-modulated signal. When transferred to time domain, this should allow the set-up to display a time-resolved electron cloud build-up, which can be compared to simulations. Since the integrated electron cloud density is directly proportional to the phase shift, a script could be programmed making an on-line calculation of the average electron cloud density. Hence, the electron cloud density could be directly monitored during scrubbing and machine development runs.

A. Appendix

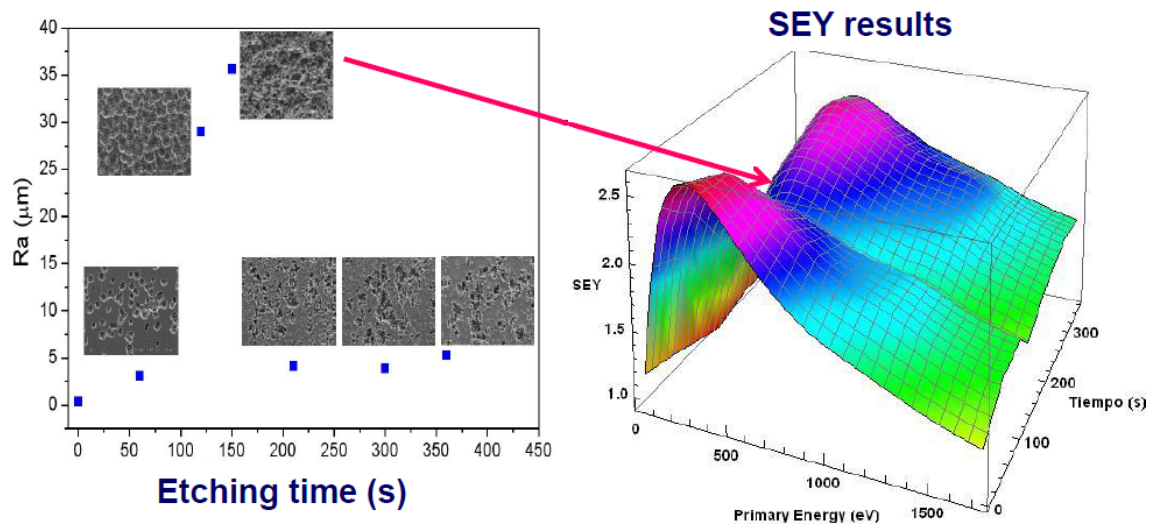


Figure A.1: Grade of the surface roughness (Ra) of aluminum versus etching time (left) and the corresponding SEY as a function of surface roughness (right). It is evident that surfaces with high roughness have a significantly lower maximum SEY. [Isabel Monterro, Presentation slides of ECLOUD'12, Elba, Italy]

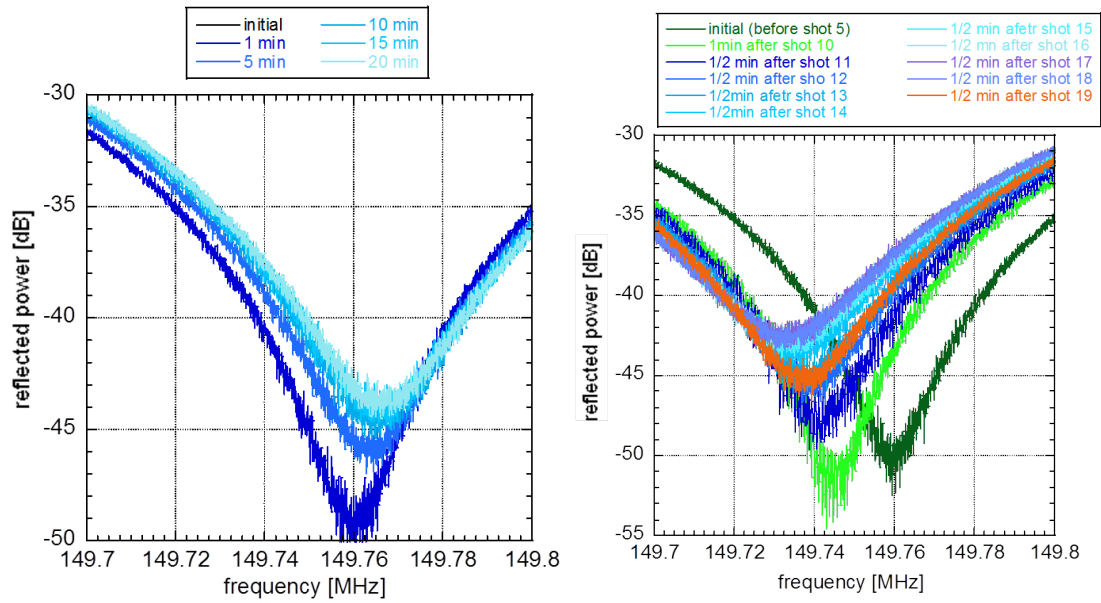


Figure A.2: Resonance drift at several time steps during measurements and the cooldown process of the wire. [P. Costa Pinto]



Figure A.3: These pictures show the opened front aperture of the pre-chamber. The rotatable device for stretching the wire can be seen, as well as the insulated transition from the wire to the RF-input, integrated in the front flange.

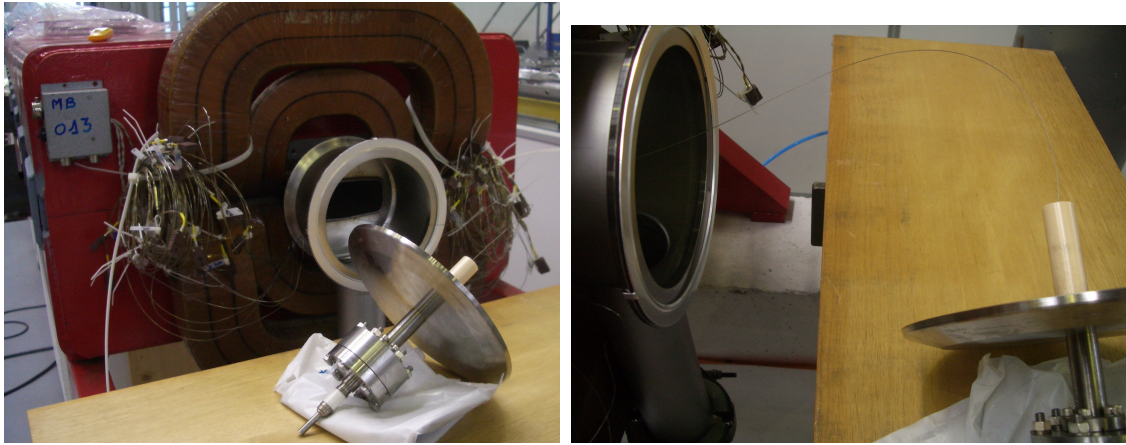


Figure A.4: These pictures show the opened back aperture of the set-up (pumping port). The tungsten wire is connected to a electrical feed trough. The part in the feed trough is insulated with a ceramic tube.

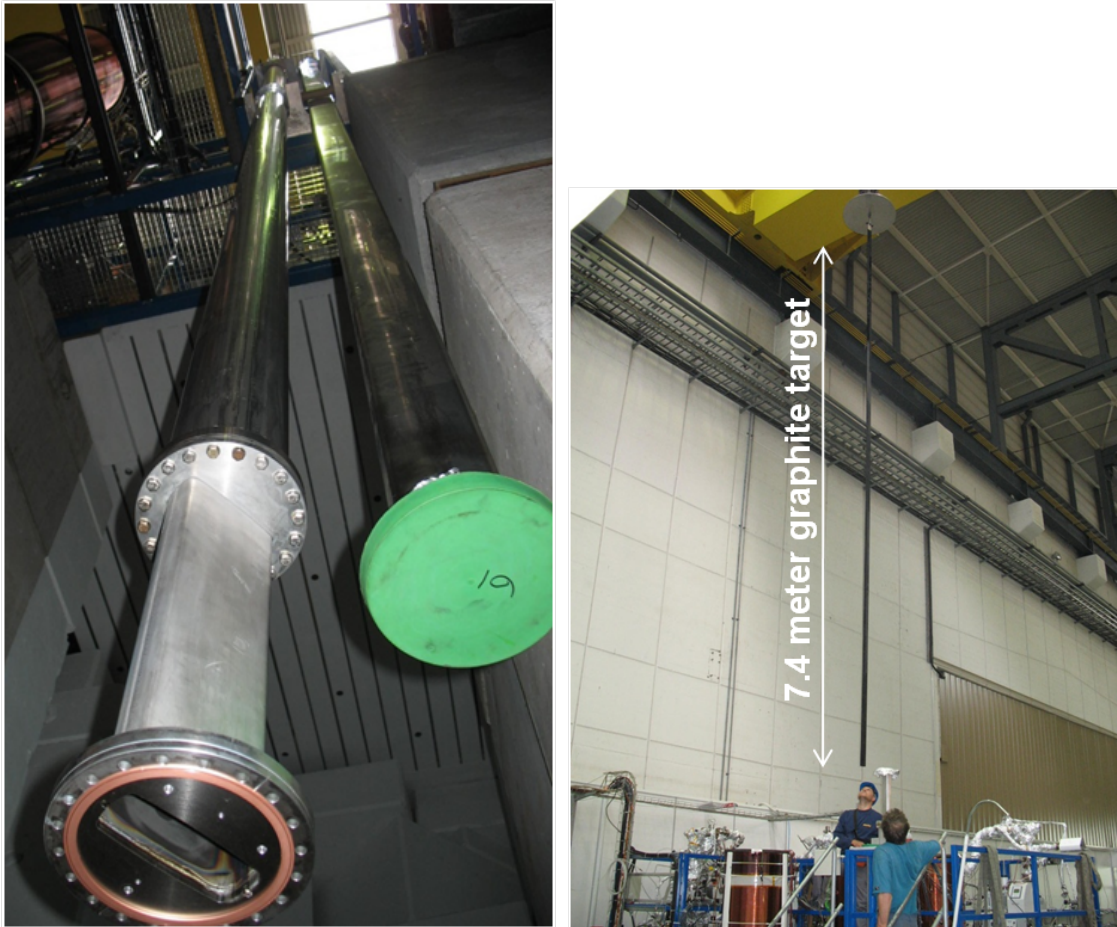


Figure A.5: Left: Extracted beam chamber after the magnet was dismantled. It is inserted in vertical solenoids. Right: Graphite target is vertically inserted into the beam chamber. [P. Costa Pinto]

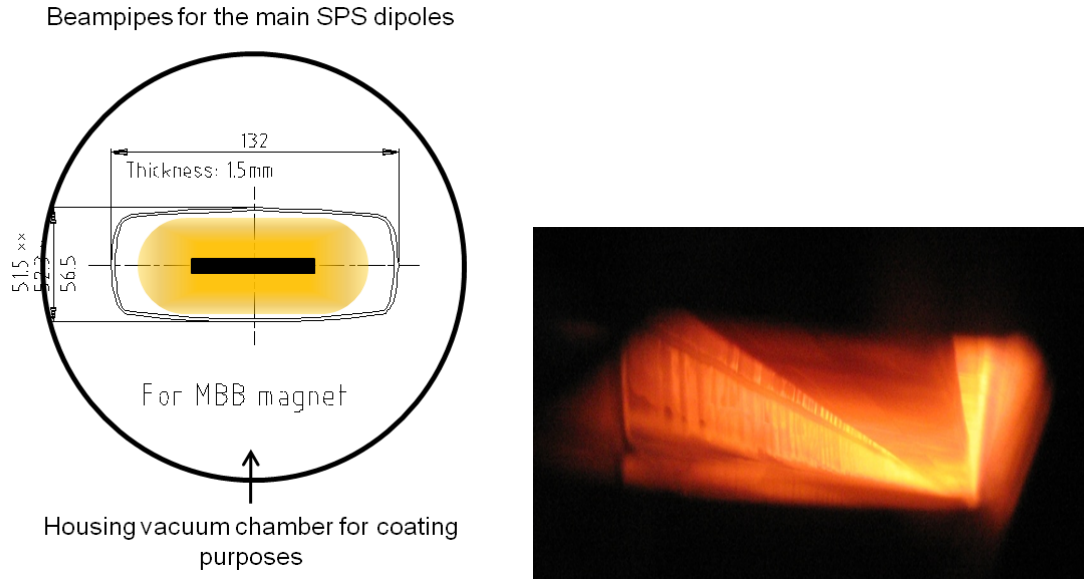


Figure A.6: Left: Scheme of the set-up for DCCM Sputtering. Right: Plasma formation during the DCCMS coating process (Neon, $8 \cdot 10^{-2}$ mbar). [P. Costa Pinto]

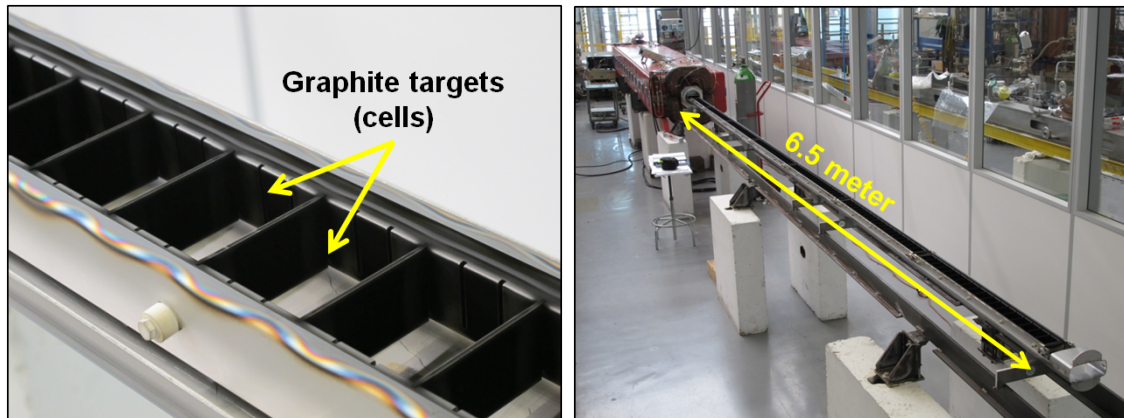


Figure A.7: Left: Graphite targets for the DCHCS coating process. Right: 6.5 meters long target liner before insertion into the beam chamber. [P. Costa Pinto]

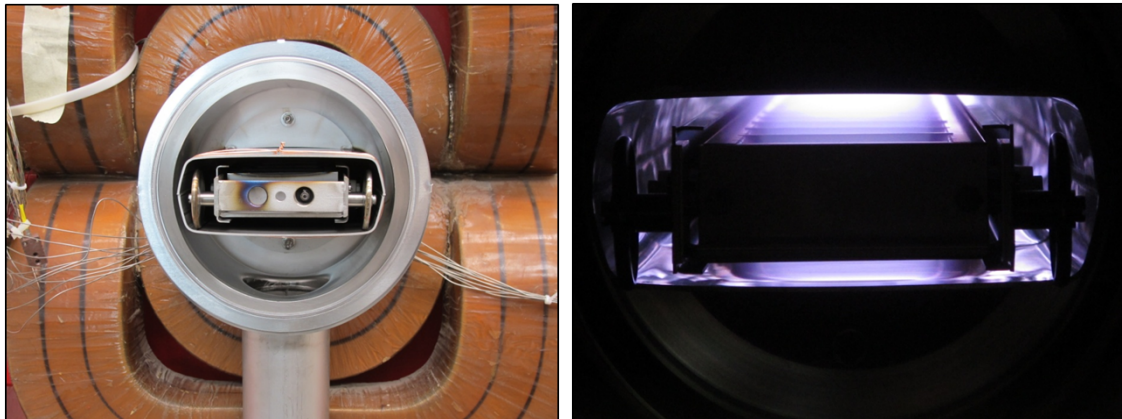


Figure A.8: Left: Inserted graphite target in the MBB-type dipole. Right: Plasma formation during the sputtering process (Argon, $2.4 \cdot 10^{-1}$ mbar). [P. Costa Pinto]

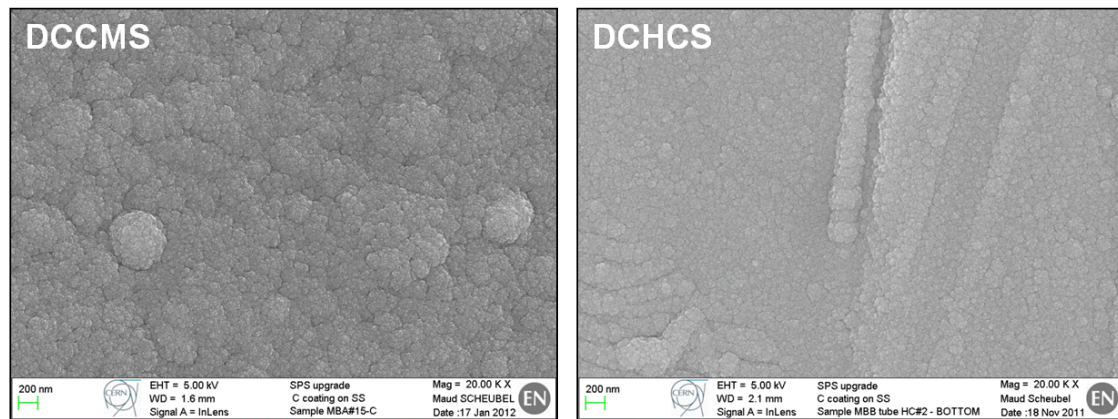


Figure A.9: Left: Surface of the DCCMS coating. Right: Surface of the DCHCS coating. [P. Costa Pinto]

Bibliography

- [1] M. Betz. Feasibility study for high power rf energy recovery in particle accelerators. CERN-THESIS-2010-125, 2010.
- [2] H. Bruining. *Physics and Applications of Secondary Electron Emission*. Pergamon Press, London, 1954.
- [3] N. Hilleret. Coefficient d’émission électronique secondaire de l’extrudal apres divers traitements. CERN Technical Note, 1983.
- [4] Mauro Taborelli. E-cloud and the effect of coatings. Presentation at the CLIC Seminar, <http://indico.cern.ch/conferenceDisplay.py?confId=55709>, last accessed 17.9.2012, 2009.
- [5] C. Yin Vallgren et al. Amorphous carbon coatings for the mitigation of electron cloud in the cern super proton synchrotron. *PHYSICAL REVIEW SPECIAL TOPICS - ACCELERATORS AND BEAMS*, 14, 2011.
- [6] W.J. Gallagher. The multipactor effect. *IEEE Transactions on Nuclear Science*, NS-26(3), June 1979.
- [7] Edward F. Vance. One-sided multipactor discharge modes. *JOURNAL OF APPLIED PHYSICS*, 34(11):3237–3242, November 1963.
- [8] Fritz Caspers, Giovanni Rumolo, Walter Scandale, and Frank Zimmermann. Beam-induced multipactoring and electron-cloud effects in particle accelerators. MULCOPIM08, 2008.
- [9] S K NAGESH, D REVANNASIDDIAH, and S V K SHASTRY. Investigation of multipactor breakdown in communication satellite microwave co-axial systems. *PRAMANA - journal of physics*, 64(1):95–110, January 2005.
- [10] Edgar Mahner, Tom Kroyer, and Fritz Caspers. Electron cloud detection and characterization in the cern proton synchrotron. *PHYSICAL REVIEW SPECIAL TOPICS - ACCELERATORS AND BEAMS*, 11, 2008.
- [11] T. Kroyer, F. Caspers, E. Metral, and F. Zimmermann. Distributed electron cloud clearing electrodes. Joint CARE-ELAN, CARE-HHH-APD, and EUROTEV-WP3 Workshop on Electron Cloud Clearing, 2007.
- [12] S. De Santis, J.M. Byrd, F. Caspers, A. Krasnykh, T. Kroyer, M.T.F. Pivi, and K.G. Sonnad. Measurement of electron clouds in large accelerators by microwave dispersion. *PHYSICAL REVIEW LETTERS*, 100(9), 2008.

- [13] M.T.F. Pivi, F.K. King, R.E. Kirby, T.O. Raubenheimer, G. Stupakov, and F. Le Pimpec. Sharp reduction of the secondary electron emission yield from grooved surfaces. SLAC-PUB-13020, 2007.
- [14] Luigi Palumbo. Space charge. CERN Accelerator School, 2005.
- [15] Robert A. Witte. *Spectrum and Network Measurements*. Prentice Hall Inc., Englewood Cliffs, New Jersey, 1991.
- [16] S. Federmann, F. Caspers, and E. Mahner. Measurements of electron cloud density in the cern super proton synchrotron with the microwave transmission method. *PHYSICAL REVIEW SPECIAL TOPICS - ACCELERATORS AND BEAMS*, 14, 2011.
- [17] M. Hiebel. Fundamentals of vector network analysis. fourth edition, 2008.
- [18] M. Holz. Introduction to the experimental multipacting test stand / operating instructions. CERN-ATS-Note-2011-103 TECH, November 2011.
- [19] ECSS-E-20-01 Working Group. Space engineering - multipaction design and test. Published by ESA Publications Division, 2003.
- [20] M.A. Furman and M.T.F. Pivi. Probabilistic model for the simulation of secondary electron emission. Technical report, Lawrence Berkeley National Laboratory, 2003. SLAC-PUB-9912, LBNL-49771.
- [21] P. Costa Pinto, S. Calatroni, P. Chiggiato, H. Neupert, W. Vollenberg, E. Shaposhnikova, M. Taborelli, and C. Yin Vallgren. Thin film coatings for suppressing electron multipacting in particle accelerators. Proceedings of 2011 Particle Accelerator Conference, New York, 2011.
- [22] P. Costa Pinto, F. Caspers, P. Edwards, M. Holz, and M. Taborelli. Multipactor for e-cloud diagnostics. IPAC2012 - Proceedings, New Orleans, 2012.
- [23] Otto Zinke and Heinrich Brunswig. *Hochfrequenztechnik 1*. Springer-Verlag, Berlin/New York, 1973.
- [24] S. De Santis, J. M. Byrd, F. Caspers, A. Krasnykh, T. Kroyer, M. T. F. Pivi, and K. G. Sonnad. Measurement of electron clouds in large accelerators by microwave dispersion. *PHYSICAL REVIEW LETTERS*, 10, 2008.
- [25] S. Federmann, F. Caspers, and E. Mahner. Measurements of electron cloud density in the cern super proton synchrotron with the microwave transmission method. *PHYSICAL REVIEW SPECIAL TOPICS - ACCELERATORS AND BEAMS*, 7, 2011.
- [26] F. Caspers, P. Costa Pinto, P. Edwards, S. Federmann, M. Holz, and M. Taborelli. Sps dipole multipactor test and te wave diagnostics. Proceedings of ECLLOUD12, Elba, Italy, to be published, 2012.